AGU ADVANCING EARTH AND SPACE SCIENCE

Tectonics

RESEARCH ARTICLE
10.1029/2020TC006482

Key Points:
- Deformation temperatures combined with thermochronometry indicate that the shearing that exhumed the Tso Morari nappe continued until ~30 Ma
- Top-to-east shearing outlasted rapid India-Asia convergence by ~15 Myr and may be a result of strain partitioning in the western Himalaya
- The exhumation of the Tso Morari nappe is generally consistent with models of UHP exhumation that emphasize piston forcing or recirculation

Supporting Information:
- Supporting Information S1
- Table S1
- Table S2
- Table S3

Correspondence to:
S. P. Long,
sean.p.long@wsu.edu

Citation:
Long, S. P., Kohn, M. J., Kerswell, B. C., Starnes, J. K., Larson, K. P., Blackford, N. R., & Soignard, E. (2020). Thermometry and microstructural analysis imply protracted extensional exhumation of the Tso Morari UHP nappe, northwestern Himalaya: Implications for models of UHP exhumation. *Tectonics*, *39*, e2020TC006482. https://doi.org/10.1029/2020TC006482

Received 18 AUG 2020
Accepted 23 NOV 2020
Accepted article online 25 NOV 2020

Thermometry and Microstructural Analysis Imply Protracted Extensional Exhumation of the Tso Morari UHP Nappe, Northwestern Himalaya: Implications for Models of UHP Exhumation

Sean P. Long[1], Matthew J. Kohn[2], Buchanan C. Kerswell[2], Jesslyn K. Starnes[1], Kyle P. Larson[3], Nolan R. Blackford[1], and Emmanuel Soignard[4]

[1]School of the Environment, Washington State University, Pullman, WA, USA, [2]Department of Geosciences, Boise State University, Boise, ID, USA, [3]Department of Earth and Environmental Sciences, University of British Columbia Okanagan, Kelowna, British Columbia, Canada, [4]LeRoy Eyring Center for Solid State Science, Arizona State University, Tempe, AZ, USA

Abstract Documenting the processes that facilitate exhumation of ultrahigh-pressure (UHP) rocks at convergent margins is critical for understanding orogen dynamics. Here, we present structural and temperature data from the Himalayan UHP Tso Morari nappe (TMN) and overlying nappes, which we integrate with published pressure-temperature-time constraints to refine interpretations for their structural evolution and exhumation history. Our data indicate that the 5.5-km-thick TMN is the upper portion of a penetratively deformed ductile slab, which was extruded via distributed, pure shear-dominated, top-down-to-east shearing. Strain in the TMN is recorded by high-strength quartz fabrics (density norms between 1.74 and 2.86) and finite strain data that define 63% transport-parallel lengthening and 46% transport-normal shortening. The TMN attained peak temperatures of ~500–600°C, which decrease in the overlying Tetraogal and Mata nappes to ~150–300°C, defining a field gradient as steep as 67°C/km. Within the overlying nappes, quartz fabric strength decreases (density norms between 1.14 and 1.21) and transport-parallel lengthening and transport-normal shortening decrease to 14% and 18%, respectively. When combined with published $^{40}Ar/^{39}Ar$ thermochronometry, quartz fabric deformation temperatures as low as ~330°C indicate that the top-to-east shearing that exhumed the TMN continued until ~30 Ma. Peak temperatures constrain the maximum depth of the overlying Mata nappe to 12.5–17.5 km; when combined with published fission-track thermochronometry, this provides further support that the TMN was not underplated at upper crustal levels until ~30 Ma. The long-duration, convergence-subnormal shearing that exhumed the TMN outlasted rapid India-Asia convergence by ~15 Myr and may be the consequence of strain partitioning during oblique convergence.

1. Introduction

Documenting the metamorphic conditions and structural processes associated with the exhumation of ultrahigh-pressure (UHP; >27 kbar) rocks can lend insights into the deformation processes that operate at upper mantle depths and can provide critical information for testing and refining models for the geodynamic evolution of orogenic belts (e.g., Chemenda et al., 1995; Hacker et al., 2013; Warren et al., 2008a). In the Himalayan orogen, rocks preserving UHP assemblages, which indicate subduction of continental rocks of the Indian plate down to ~100-km depths, have been exhumed in northern Pakistan (e.g., Rehman et al., 2008; Wilke et al., 2010) and northwestern India (e.g., de Sigoyer et al., 2000; Epard & Steck, 2008; Guillot et al., 1997; Leech et al., 2005, 2007; Schlup et al., 2003; St.-Onge et al., 2013). In northwestern India (Figure 1), rocks exposed in the Tso Morari nappe (TMN) preserve evidence for attaining peak pressures of ~27 kbar (or greater) by ~54–51 Ma, followed by exhumation to ~7–10 kbar by ~48–46 Ma, which has been interpreted to represent a record of subduction, detachment, and extrusion of rocks of the leading edge of the Indian plate, all within ~10 Myr of initial India-Asia collision (e.g., de Sigoyer et al., 2000, 2004; Donaldson et al., 2013; Epard & Steck, 2008; Leech et al., 2005, 2007; St.-Onge et al., 2013). Therefore, the Tso Morari region represents an important locality for investigating the processes that accommodate the exhumation

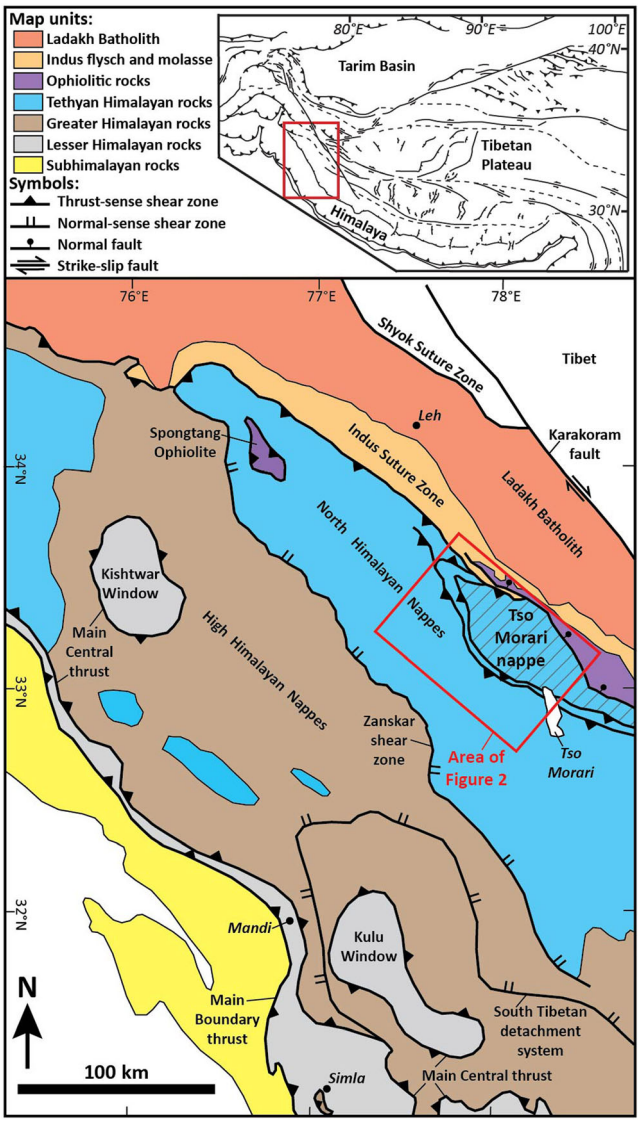

Figure 1. Simplified geologic map of part of the northwestern Himalaya, modified from Horton et al. (2015) and St.-Onge et al. (2013). Inset map of the Himalayan-Tibetan orogen is modified from Horton et al. (2015).

of rocks buried to upper mantle depths and has the potential to provide critical insights into the evolution of the earliest Himalayan deformation.

Investigations of the metamorphic conditions and timing of eclogite facies UHP metamorphism in the TMN, as well as the Barrovian-style amphibolite facies metamorphism that occurred at midcrustal depths along its exhumation path (e.g., de Sigoyer et al., 2000; Girard, 2001; Guillot et al., 1997; Leech et al., 2005, 2007; Pan et al., 2020; Schlup et al., 2003; St.-Onge et al., 2013), have provided foundational P-T-t datapoints that have informed regional tectonic models for the geodynamic evolution of the nappe (most notably de Sigoyer et al., 2004; Epard & Steck, 2008). These burial-exhumation histories and models, in turn, have served to inform broader discussions of UHP metamorphism (e.g., Beaumont et al., 2009; Chopin, 2003; Hacker et al., 2013; Kylander-Clark et al., 2012). However, several key questions remain regarding the geometry, kinematics, and style of the structures that helped accommodate the extrusion of the TMN, as well as the metamorphic and structural history of the rocks that the TMN was emplaced beneath, which consist of metasedimentary rocks of the North Himalayan nappes (Figure 1). These gaps in our knowledge limit our ability to use the structural and metamorphic history of the TMN to develop a better understanding of Himalayan tectonics specifically and of the metamorphism and exhumation of UHP rocks in general.

The overall goal of this study is to better understand the exhumation process of UHP rocks, using the TMN as a case study. Specific questions that we address include the following: How high up in the crust do UHP rocks exhume via extensional shearing during their initial ascent? How consistent are inferred P-T-t paths with published models of UHP formation and exhumation? How do subsequent large-scale orogenic processes impact the post-UHP metamorphic and structural evolution? To address these questions, we refine models for the structural evolution and exhumation history of three transects through the TMN and the overlying North Himalayan nappes. Throughout these transects, we have collected peak temperatures determined via Raman spectroscopy of carbonaceous material (RSCM) thermometry, quartz crystallographic preferred orientations (CPOs), microscale 3D finite strain analyses, and shear-sense observations. We use these data to define spatial trends in kinematics, peak and deformation temperature, strain magnitude, kinematic vorticity, and the strength of CPO development. These data allow for interpretations about the depths and temperatures at which extensional exhumation ceased. We combine our data with published work on peak pressures, overprinting amphibolite facies P-T conditions, and local to regional geo- and thermochronology, in order to compare our results to published models for UHP P-T-t evolution. Finally, we re-evaluate the overall tectonic evolution of the TMN in the context of post-UHP deformation and metamorphism of the underlying Himalayan metamorphic core.

2. Regional Tectonic Framework

The Himalayan-Tibetan orogen has formed from progressive deformation associated with the initial Paleocene-Early Eocene collision of India and Asia that marked the closure of the Neotethys Ocean and the continued convergence that has followed (e.g., Gansser, 1964; LeFort, 1975; Yin, 2006). In the portion of the orogen in northwestern India (Figure 1), prior to initial plate collision, the southern Asian margin consisted of the Cretaceous-Paleogene Ladakh Batholith, a magmatic arc that formed above northward-subducting Tethyan oceanic lithosphere (e.g., Honegger et al., 1982; Singh et al., 2007; Weinberg & Dunlap, 2000). The protoliths of the TMN consist of sedimentary rocks of the Tethyan Himalayan package that were deposited on the northern, leading edge of the Indian continent between the

Neoproterozoic and Mesozoic, intruded by granites during the Ordovician and mafic dikes during the Permian, and subducted beneath the Asian plate during the Eocene (Epard & Steck, 2008; Steck et al., 1998).

Not all data and interpretations converge on a consistent UHP P-T-t history for the TMN; many argue for a depth of ~100 km at ~600°C between ~54 and ~51 Ma (e.g., de Sigoyer et al., 2000; Leech et al., 2005, 2007; St.-Onge et al., 2013), while others argue for depths up to ~160 km at ~650–750°C with ages as young as ~45 Ma (Donaldson et al., 2013; Mukherjee et al., 2003; Wilke et al., 2015), and still others point to large P-T differences depending on what type of thermodynamic modeling is applied (Pan et al., 2020). Post-UHP detachment and extrusion of the TMN at rates of 1.2 (St.-Onge et al., 2013) to 12 cm/yr (Wilke et al., 2015) are interpreted to have been facilitated by its low density relative to surrounding mantle peridotites (Chatterjee & Jagoutz, 2015; de Sigoyer et al., 2004; Epard & Steck, 2008) and accommodated by top-down-to-east shearing within the TMN (Epard & Steck, 2008). Coeval with early exhumation of the TMN, the initial detachment and south-vergent stacking of thrust sheets of upper crustal, Neoproterozoic-Mesozoic Tethyan Himalayan rocks began to construct the North Himalayan nappes between ~53 and ~48 Ma (Epard & Steck, 2008).

Following emplacement of the TMN beneath the North Himalayan nappes by ~48 Ma (Epard & Steck, 2008), continued exhumation was accompanied by amphibolite facies metamorphism that affected both the TMN and overlying nappes. The estimated P-T conditions and timing of this metamorphism in the TMN are ~500–750°C and ~7–10 kbar at ~48–45 Ma (de Sigoyer et al., 2000, 2004; Epard & Steck, 2008; Girard, 2001; St.-Onge et al., 2013; Wilke et al., 2015), although there are no quantitative estimates of P-T conditions available for rocks in the overlying nappes. Following this metamorphism, muscovite and biotite $^{40}Ar/^{39}Ar$ and zircon fission-track ages show that the TMN cooled through ~425–240°C between ~45 and ~29 Ma, and apatite fission-track ages indicate cooling through ~120°C between ~26 and ~8 Ma (de Sigoyer et al., 2000; Schlup et al., 2003). This cooling is attributed to exhumation during continued deformation, including southwest-directed thrust stacking of the North Himalayan nappes, passive rock uplift accompanying thrust belt development in the foreland to the southwest, and northeast-directed thrusting and folding in the Indus Suture Zone to the north (Epard & Steck, 2008; Steck et al., 1993; Stutz & Steck, 1986).

3. Tectonostratigraphy of the Tso Morari Region

3.1. Tectonostratigraphic Divisions From Previous Work

Mapping-based studies over the past two decades have developed a detailed structural and tectonostratigraphic framework for the Tso Morari Region (e.g., Buchs & Epard, 2019; Epard & Steck, 2008; Steck et al., 1998). From the lowest to the highest, three structural packages have been defined: the TMN, Tetraogal nappe, and Mata nappe (Figure 2).

The TMN consists of granitic orthogneiss interlayered with schist, marble, and quartzite, which are interpreted as metamorphosed equivalents of Neoproterozoic-Cambrian Tethyan Himalayan sedimentary rocks (the Haimantas and Karsha Formation) exposed throughout the region (e.g., Draganits et al., 1998; Nanda & Singh, 1977; Steck et al., 1998). The orthogneiss (variably called the "Tso Morari granite," "Tso Morari gneiss," or "Puga orthogneiss" in earlier studies) is interpreted to represent an Ordovician (479 ± 2 Ma; U-Pb zircon; Girard & Bussy, 1999) granite that intruded Tethyan Himalayan sedimentary rocks. The orthogneiss commonly contains boudins of eclogitic metabasite that are up to 3 m thick, which are interpreted to represent syn-granitic mafic dikes (e.g., Epard & Steck, 2008). Thermobarometric studies of these eclogitized boudins have provided evidence for burial of the TMN to at least ~27 kbar (e.g., Bidgood et al., 2020; Pan et al., 2020; Sachan et al., 2004; St.-Onge et al., 2013). Metasedimentary rocks are also present in the TMN, including intercalated metapelites and metapsammites. Typical muscovite + plagioclase + quartz-bearing assemblages in the orthogneiss and metasediments would have melting temperatures of ~650°C (water present) or ~700°C (water absent) (e.g., Spear et al., 1999). However, we observed no definitive evidence for partial melting in the TMN. A single exception (Stop 22, near the village of Puga) may represent melt injection rather than in situ melting.

Overlying the TMN, a ~0.5- to 3-km-thick package of metasedimentary Tethyan Himalayan rocks, which includes schist, phyllite, quartzite, marble, and metavolcanics, has been interpreted as a thin, thrust-bound horse called the Tetraogal nappe (Figure 2) (Steck et al., 1998). The protoliths of the

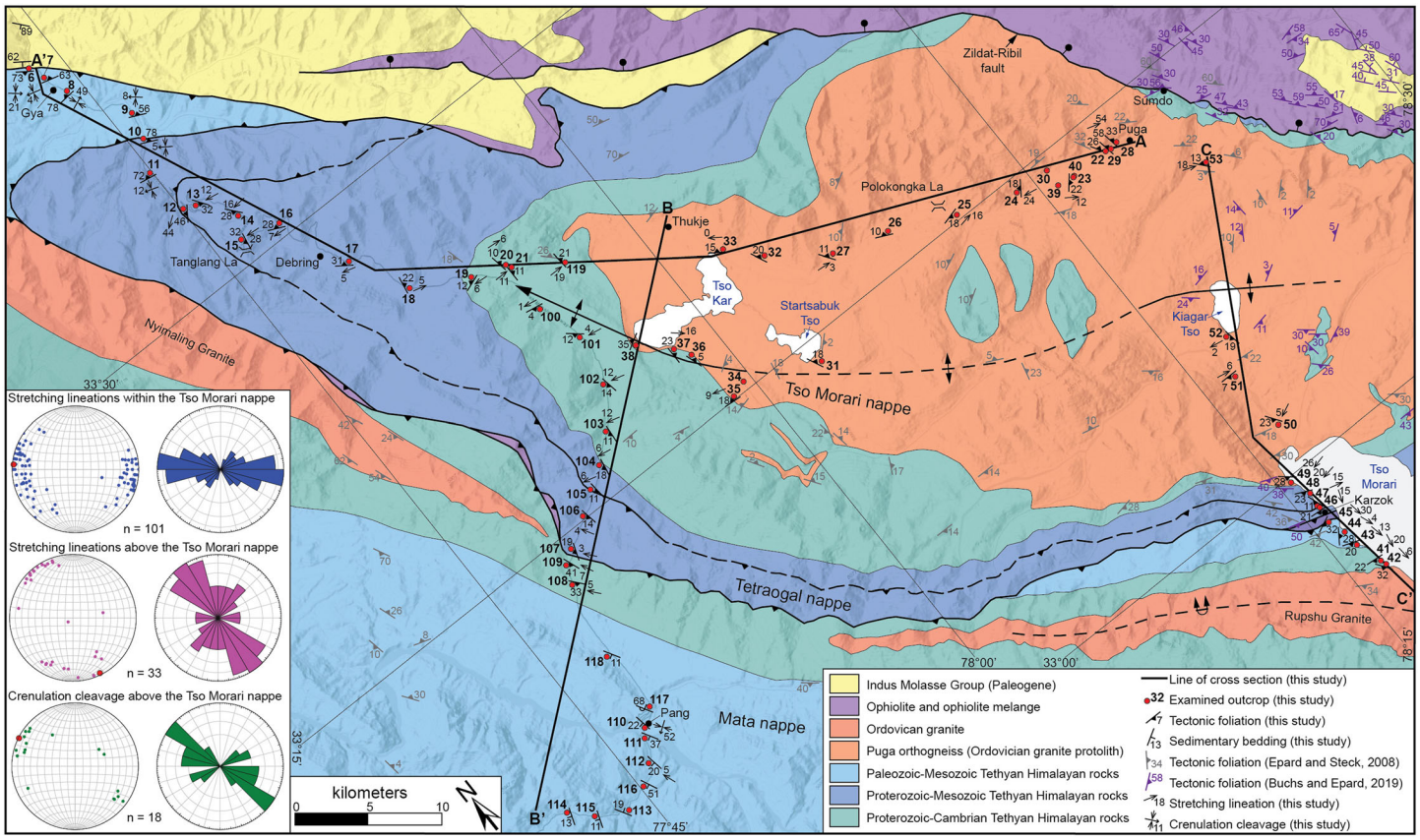

Figure 2. Geologic map of the Tso Morari region. Sources of map data include Buchs and Epard (2019), Epard and Steck (2008), and this study. The upper contact of the TMN was mapped at the highest occurrence of prevalent E-W-trending mineral stretching lineations and represents the top of a zone of distributed shearing. Inset on the lower left shows stereoplots and rose diagrams of mineral stretching lineations and crenulation cleavage measurements (generated using Orient).

metasedimentary rocks in the Tetragoal nappe are interpreted to have been deposited between the Permian and Cretaceous (de Sigoyer, 1998; Fuchs & Linner, 1996; Steck et al., 1998; Virdi et al., 1978). Metabasites are present locally in the Tetraogal nappe and are interpreted to represent deformed dolerite dikes (Steck et al., 1998). These metabasites, however, lack the eclogitic assemblages observed in the TMN, which was a primary reason for interpreting the Tetraogal nappe as a separate tectonostratigraphic unit (Epard & Steck, 2008).

The Mata nappe sits structurally above the Tetraogal nappe (Figure 2) and consists of >7 km of greenschist facies to unmetamorphosed Tethyan Himalayan sedimentary rocks, including slate and meta-sandstone of the Neoproterozoic-Cambrian Haimantas and Cambrian Karsha Formation, and Paleozoic to Cretaceous slate and limestone (e.g., Epard & Steck, 2004, 2008; Steck et al., 1998). Neoproterozoic-Cambrian metasedimentary rocks in the Mata nappe are intruded by Ordovician granite bodies that are tens of kilometers in map length (Figure 2), including the 482.5 ± 1 Ma Rupshu Granite (Girard & Bussy, 1999) and the 460 ± 8 Ma Nyimaling Granite (Stutz & Thöni, 1987). In most places in the study region, the thrust contact between the Mata and Tetraogal nappes exhibits an older-over-younger relationship, with Neoproterozoic-Cambrian Tethyan Himalayan rocks overlying Tethyan Himalayan rocks with interpreted Permian-Cretaceous protoliths (Steck et al., 1998). In addition, exposures of serpentinite, metagabbro, and metabasite mapped locally along the thrust contact between the Tetraogal and Mata nappes (Figure 2) have been interpreted as horses of metamorphosed ophiolitic rocks (Berthelsen, 1953; Buchs & Epard, 2019; Epard & Steck, 2008; Steck et al., 1998).

3.2. Mapping Transects

We performed geologic mapping and sampling along three transects that cross the TMN, Tetraogal nappe, and Mata nappe (Figure 2), including a NW trending, approximately strike-parallel transect (A-A′), and

10.1029/2020TC006482

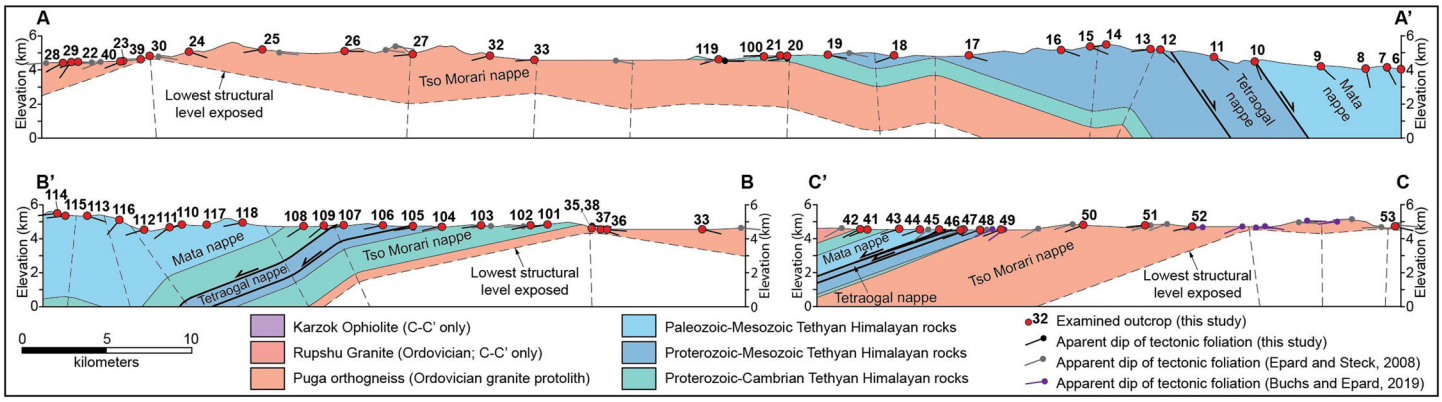

Figure 3. Cross sections of our three mapped transects (lines of section shown on Figure 2). Areas that exhibit similar apparent dip of tectonic foliation were divided into dip domains, which are separated by kink axes that bisect the interlimb angle (e.g., Suppe, 1983).

two NE trending, approximately strike-normal transects (B-B′ and C-C′). A total of 68 outcrops were examined, with samples collected for thin sections at 56 of these localities (see Table S1 in the supporting information). Structural (i.e., foliation-normal) thicknesses were measured for each transect by projecting the apparent dip of tectonic foliation measurements onto cross sections (Figure 3), and the structural positions of all examined outcrop localities for each transect are projected onto tectonostratigraphic columns (Figure 4).

Mesoscopic deformation fabrics, including tectonic foliation and mineral stretching lineations, are ubiquitous at lower structural levels but become progressively less common or die out altogether with increasing structural height. At the lowest structural levels (which correspond to the full exposed thickness of the TMN and the basal part of the Tetraogal nappe, as mapped by Steck et al., 1998), all examined rocks exhibit prevalent E-W-trending mineral stretching lineations (275° average azimuth; Figure 2 inset). Structurally upward (within the upper part of the Tetraogal nappe and the Mata nappe, as mapped by Steck et al., 1998), mineral stretching lineations are much less common and are variable in orientation, trending either to the northwest, south, or southwest, with the most common trend of 315–330° (Figure 2 inset). Within the structurally highest ~2 km of the Mata nappe examined on transect B-B′, neither planar nor linear deformation fabrics were observed, and primary sedimentary bedding in limestone is the dominant mesoscopic feature (Figure 2).

Here, and in the following sections, we present field observations and data sets that support reinterpretation of the lower part of the Tetraogal nappe as part of the TMN. The full exposed thickness of the TMN and the basal part of the Tetraogal nappe as mapped by Steck et al. (1998) exhibit prevalent E-W-trending mineral stretching lineations. We interpret that these rocks represent a genetically related zone of distributed, intense penetrative shearing within the top of the TMN. This interpretation is supported by an abrupt upward transition to variably oriented, more sparsely distributed mineral stretching lineations and overall lower metamorphic grades in overlying rocks. On the tectonostratigraphic columns of our three transects (Figure 4), structural heights are listed in reference to the top of the zone of prevalent E-W-trending mineral stretching lineations (i.e., the top of the TMN, as we define it). All structural heights in the following text are listed in meters below (negative values) or above (positive values) this structural level. In the following paragraphs, we describe lithologies observed on each of our three transects.

1. Transect A-A′: Granitic orthogneiss is exposed between −5,600 and −2,850 m (Stops 22–33 and 39–40) and is interlayered with marble and biotite-garnet schist between −3,450 and −2,850 m (Stops 19–21, 100, and 119). These rocks transition upward to biotite-garnet schist, quartzite, metabasite, phyllite, and marble between −2,850 and 0 m (Stops 12–18); this interval was mapped as the basal part of the Tetraogal nappe by Steck et al. (1998), but based on prevalent E-W-trending lineations, we map these rocks as part of the TMN (Figure 2). The structurally highest biotite porphyroblasts and garnet observed on this transect are at −2,850 m (Stop 18). Moving structurally upward, the Tetraogal nappe consists of interlayered limestone and crenulated phyllite (Stops 10 and 11) between 0 and 3,800 m, and the Mata

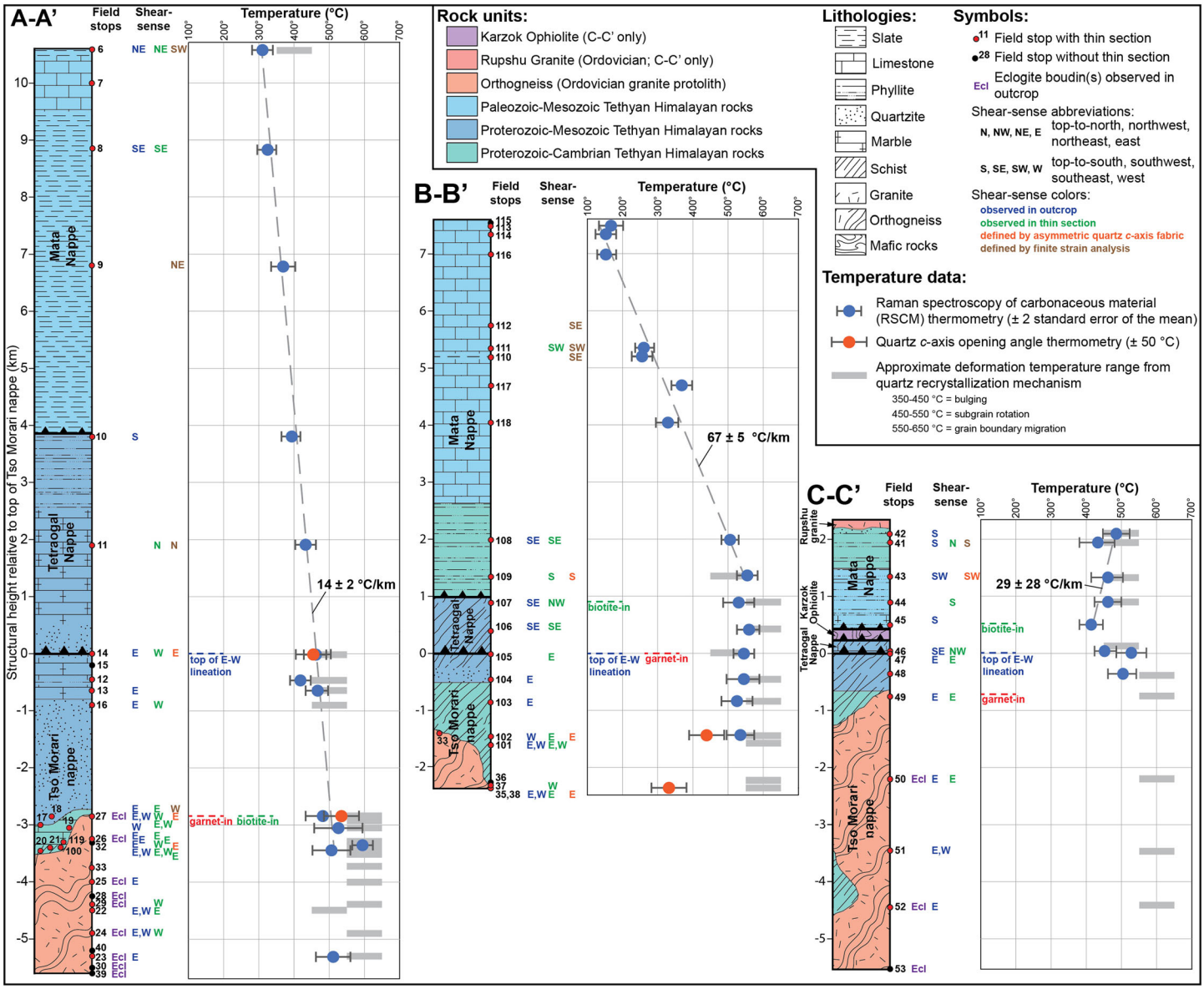

Figure 4. Tectonostratigraphic columns of our three mapped transects (calculated from structural thicknesses on Figure 3), plotting structural height relative to the top of the TMN (i.e., at the top of the zone of prevalent E-W-trending mineral stretching lineations). Field stops are plotted, as well as shear-sense observations, temperature data, and mineral isograds.

nappe consists of interlayered graphitic phyllite and slate (Stops 6, 8, and 9) and limestone (Stop 7) between 3,800 and 10,600 m.

2. Transect B-B′: Orthogneiss is interlayered with Neoproterozoic-Cambrian metasedimentary rocks between −2,350 and −1,400 m (Stops 33, 35, 37, and 38). Metasedimentary rocks between −2,350 and −1,150 m consist of biotite-garnet schist (Stops 36, 101, and 102) and are overlain by biotite-garnet-hornblende schist interlayered with quartzite between −1,150 and 0 m (Stops 103–105). The interval between −500 and 0 m was mapped as the basal part of the Tetraogal nappe by Steck et al. (1998), but based on E-W-trending lineations, we map these rocks as part of the TMN. The structurally highest garnet observed on this transect is at 0 m (Stop 105). The Tetraogal nappe between 0 and 1,000 m consists of biotite-hornblende schist (Stops 106 and 107). The structurally highest biotite porphyroblasts observed on this transect are at 900 m (Stop 107). The Mata nappe consists of muscovite-chlorite phyllite between 1,000 and 2,600 m (Stops 108 and 109), which is overlain by limestone interlayered with lineated or

crenulated slate between 2,600 and 5,500 m (Stops 110, 111, 117, and 118), and undeformed limestone between 5,500 and 7,600 m, which does not exhibit planar or linear deformation fabrics (Stops 113–116).

3. Transect C-C′: Relative to other areas of the TMN, rocks along this transect have been disproportionately studied for petrology and geochronology (e.g., de Sigoyer et al., 1997, 2000; Donaldson et al., 2013; Gouzu et al., 2006; Leech et al., 2005, 2007; O'Brien, 2018; Palin et al., 2014; Pan et al., 2020; Sachan et al., 2004; Schlup et al., 2003; St.-Onge et al., 2013; Wilke et al., 2015). Garnet-bearing orthogneiss with sparse, eclogitic mafic boudins is exposed between −5,500 and −650 m (Stops 49–53). The structurally highest garnet observed on this transect is within orthogneiss at −750 m (Stop 49). Above the orthogneiss, biotite-rich schist is exposed between −650 and 0 m; these rocks were mapped as the base of the Tetraogal nappe by Steck et al. (1998), but we map them as part of the TMN based on prevalent E-W-trending lineations. Structurally above these rocks, the Tetraogal nappe consists of interfingering marble and biotite-muscovite schist between 0 and 225 m (Stop 46). The Karzok ophiolite, consisting of serpentinite, metagabbro, and metabasite, is exposed in the thrust zone between the Tetraogal and Mata nappes between 225 and 425 m (Buchs & Epard, 2019; Epard & Steck, 2008; Steck et al., 1998). The portion of the Mata nappe that we examined lies within the overturned lower limb of a recumbent fold (Figure 2) (Steck et al., 1998) and consists of interlayered graphitic phyllite, marble, and quartzite between 425 and 2,200 m (Stops 41–45). The structurally highest biotite porphyroblasts observed on this transect are at 500 m (Stop 45). The Ordovician Rupshu Granite is exposed at the top of our examined section, between 2,200 and 2,300 m.

4. Shear-Sense Observations

Shear-sense indicators were observed on all three transects, at a total of 36 outcrops and within thin sections from 31 outcrops (Figure 4). Outcrop- and thin section-scale shear-sense indicators that we observed included (in order of most common to least common) rigid mineral clasts and boudins sheared into σ-objects, C-type shear bands (i.e., SC fabrics), oblique secondary foliations in recrystallized quartz or calcite, C′-type shear bands, asymmetric folds (with axes that trend subnormal to lineation), mica fish, and asymmetric boudinage (Figures 5 and 6).

In addition to these observations, seven quartz fabric samples exhibit asymmetric CPOs that define shear sense (discussed below in section 7), and nine finite strain analyses yielded mean quartz grain elongation directions that define shear sense (discussed below in section 8). Combining all shear-sense data from outcrops, thin sections, quartz fabrics, and strain analyses defines mixed kinematics at 17 individual examined field stops (Figure 4), including 13 field stops in the TMN that exhibit both top-to-east and top-to-west shear senses (examples highlighted in Figures 5c and 5d, 6b and 6c, and 6d and 6e), and two field stops each in the Tetraogal and Mata nappes that exhibit both southward and northward shear components. However, graphing all shear-sense observations ($n = 95$) in a histogram versus structural height (Figure 7) defines the dominant trends in shear sense. Within the TMN ($n = 63$), top-to-east and top-to-west shear sense indicators are distributed through the full examined structural thickness. However, top-to-east indicators are dominant at all structural levels ($n = 45$) and are 2.5 times more abundant than top-to-west indicators ($n = 18$). This is similar to the observations of Dutta and Mukherjee (2020), who also documented an overall dominant top-to-east shear sense within the TMN, with local outcrops that exhibit both top-to-east and top-to-west shear senses. In the Tetraogal and Mata nappes ($n = 32$), shear-sense directions exhibit more variation, as a consequence of differing lineation orientations (Figure 2 inset). Shear-sense indicators with a component of motion toward the south (including top-to-south, southwest, or southeast) and with a component of motion toward the north (including top-to-north, northwest, or northeast) are observed through the full examined structural thickness of the Tetraogal and Mata nappes. However, a top-to-south component of shear is dominant at all structural levels of both nappes, by a factor of three ($n = 24$ vs. $n = 8$).

5. RSCM Thermometry

To calculate peak metamorphic temperatures using the RSCM thermometer (e.g., Beyssac et al., 2002, 2003; Rahl et al., 2005), we analyzed carbonaceous material from polished thin sections of 36 metasedimentary samples collected from our three transects, including 13 samples from A-A′, 15 samples from B-B′, and eight samples from C-C′ (Table 1; Figure 8). Measurements were made at Arizona State University (see Supporting

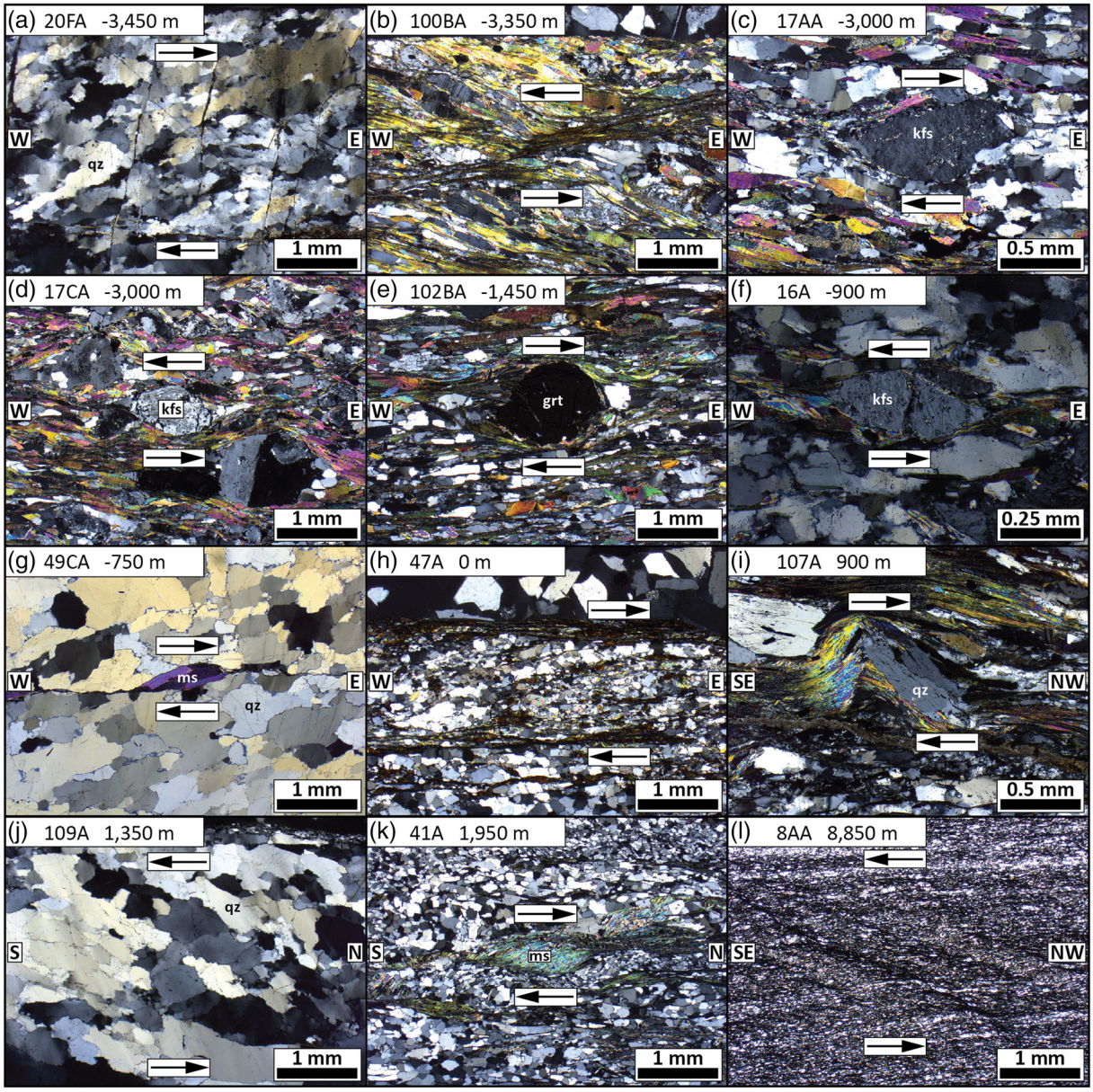

Figure 5. Examples of representative thin section-scale shear-sense indicators from lineation-parallel thin sections on all three transects, organized from structurally low to high. All photomicrographs were taken in cross-polarized light; mineral abbreviations after Whitney and Evans (2010). (a) Top-to-east oblique secondary foliation in recrystallized quartz (top and bottom of photo are oriented parallel to primary mesoscopic foliation in sample). (b) Top-down-to-west C′-type shear band, which defines an overall top-to-west shear sense. (c) Top-to-east feldspar σ-clast. (d) Top-to-west feldspar σ-clast (from same outcrop as C). (e) Top-to-east garnet σ-clast. (f) Top-to-west feldspar σ-clast. (g) Top-to-east mica fish along with top-to-east oblique secondary foliation in recrystallized quartz (top and bottom of photo are oriented parallel to primary mesoscopic foliation in sample). (h) Top-to-east C-type shear band (i.e., SC fabric). (i) Top-to-northwest rotated quartz rigid clast. (j) Top-to-south oblique secondary foliation in recrystallized quartz (top and bottom of photo are oriented parallel to primary mesoscopic foliation in sample). (k) Top-to-north mica fish. (l) Top-to-southeast C-type shear band (i.e., SC fabric).

Information S1 for supporting data and additional details on analytical methods). Representative photomicrographs of analyzed carbonaceous material, as well as examples of individual Raman spectra for each sample, are shown in Figure 8. We followed the methods of Rahl et al. (2005), in which the RSCM thermometer for rocks that achieved peak temperatures between ~100°C and ~740°C was determined by measuring the height ratio (R1) and area ratio (R2) of four first-order Raman peaks (G, D1, D2, and D3) in the relative wavenumber range of 1,200–1,800 cm^{-1}. Mean peak temperatures of multiple measurements (typically between 13 and 16 individual spots per sample; Table 1) are reported at a two standard error of

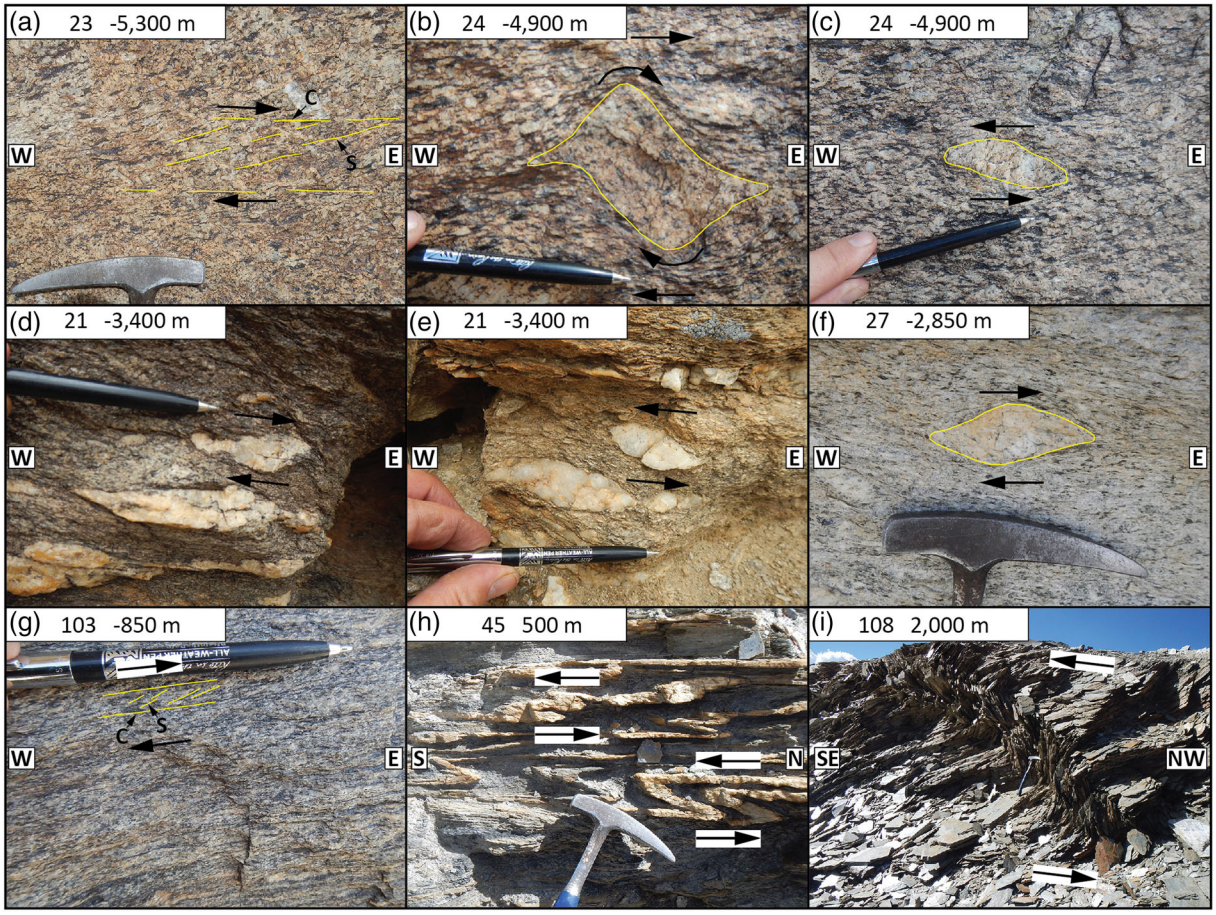

Figure 6. Examples of representative outcrop-scale shear-sense indicators from lineation-subparallel view planes on all three transects, organized from structurally low to high. (a) Top-to-east C-type shear band (i.e., SC fabric). (b) Top-to-east feldspar δ-clast. (c) Top-to-west feldspar σ-clast (from same outcrop as B). (d) Top-to-east feldspar σ-clast. (e) Top-to-west feldspar σ-clast (from same outcrop as D). (f) Top-to-east feldspar σ-clast. (g) Top-to-east C-type shear band (i.e., SC fabric). (h) Top-to-south asymmetric folds (fold axes are approximately east-west-trending and stretching lineation is south-trending, 172°). (i) Top-to-southeast asymmetric fold (fold axis is approximately southwest-trending, and stretching lineation is northwest-trending, 316°).

the mean (SEM) level, which includes the external uncertainty from the Rahl et al. (2005) calibration and the internal uncertainty from our measurements. At 2 SEM, typical error ranges for our analyzed samples are on the order of ± 25–50°C (Table 1; Figure 4).

On transect A-A′, the lowest samples from the TMN (−5,300 to −3,300 m) yielded RSCM temperatures that overlap within uncertainty between ~505°C and ~595°C (Figure 4). Above this, temperatures in the TMN decrease upward from ~480°C at −2,850 m to ~420–465°C between −650 and 0 m. Farther structurally upward, samples from the Tetraogal nappe yielded temperatures of ~435°C at 1,900 m and ~390°C at 3,800 m, and samples from the Mata nappe yielded temperatures of ~370°C at 6,800 m, ~325°C at 8,850 m, and ~310°C at 10,600 m. Collectively, RSCM data from A-A′ define a trend of upward-decreasing temperatures between −3,300 and 10,600 m that is best fit by an upright field gradient of 14 ± 2°C/km (mean square weighted deviation [MSWD] = 1.2; Figure 4). No obvious abrupt changes in temperature were observed across mapped shear zones.

On transect B-B′, seven samples that span the TMN, Tetraogal nappe, and the basal part of the Mata nappe (−1,450 to 1,350 m) yielded RSCM temperatures that overlap within uncertainty between ~525°C and ~555°C (Figure 4). Moving structurally upward through the Mata nappe, temperatures yielded by nine samples decrease systematically from ~555°C at 1,350 m to ~150–170°C at 7,000–7,500 m. This trend is best fit by a steep, upright field gradient of 67 ± 5°C/km (MSWD = 4; Figure 4).

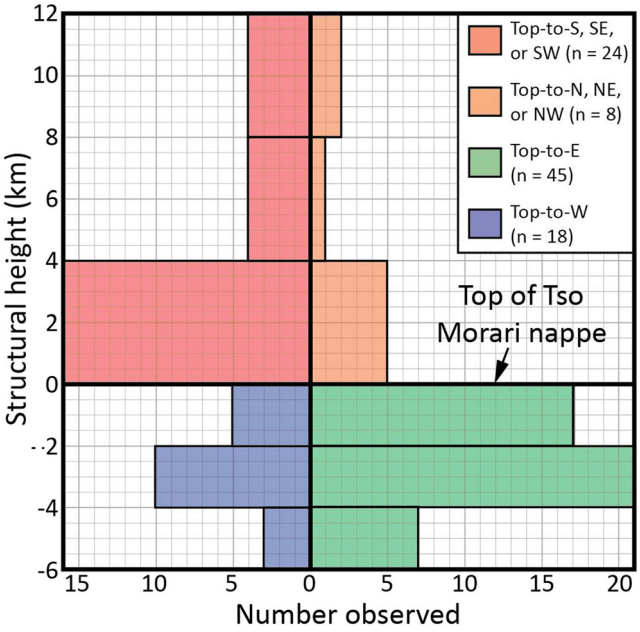

Figure 7. Frequency histogram of shear-sense indicators observed (includes outcrop- and thin section-scale observations, asymmetric quartz CPOs, and finite strain analyses) versus structural height relative to the top of the Tso Morari nappe.

On transect C-C′, samples from the TMN yielded temperatures of ~505°C at −350 m and ~530°C at 0 m. Above this, a sample from the Tetraogal nappe yielded a temperature of ~455°C at 50 m. In the Mata nappe, which lies within the overturned lower limb of a recumbent fold, five samples between 500 and 2,100 m exhibit an upward increase in temperature from ~415°C to ~490°C; this trend is best fit by an inverted field gradient of 29 ± 28°C/km (MSWD = 1.7; Figure 4). This implies that construction of the overturned fold postdated the attainment of peak temperatures in the Mata nappe.

6. Quartz Recrystallization Microstructures

Textures characteristic of dynamic recrystallization of quartz were observed in all thin sections from the TMN, in approximately half of the thin sections from the Tetraogal nappe, and in thin sections from the basal part of the Mata nappe (Figure 4). We examined the morphology of recrystallized quartz in these thin sections to interpret the dominant recrystallization mechanism and estimate approximate deformation temperature ranges (e.g., Law, 2014; Stipp et al., 2002). We utilized the deformation temperature ranges suggested by Law (2014) for Himalayan rocks, which are plotted on Figure 4. Because the mechanisms of quartz recrystallization are dependent on several other factors, including strain rate and water content (e.g., Law, 2014), we cautiously interpret these deformation temperature ranges as approximate constraints, which are shown largely for comparison with our quantitative temperature data sets.

Three different recrystallization microstructures were observed: (1) amoeboid quartz grains up to ~0.5–1.5 mm in diameter (Figures 9a and 9b; e.g., Guillope & Poirier, 1979; Urai & Lister, 1986), representing grain boundary migration at deformation temperatures of ~550–650°C (Law, 2014); (2) equigranular textures of ~0.05- to 0.1-mm diameter quartz grains (Figures 9c and 9d; e.g., Poirier & Nicolas, 1975; White, 1977), representing subgrain rotation at deformation temperatures of ~450–550°C (Law, 2014); and (3) $\lesssim$0.05-mm diameter bulges or subgrains localized at the boundaries of relict (i.e., detrital) quartz clasts (Figure 9e; Bailey & Hirsch, 1962; Drury et al., 1985), representing bulging recrystallization at deformation temperatures of ~350–450°C (Law, 2014).

The quartz recrystallization observations highlight an overall pattern of decreasing deformation temperature moving structurally upward. On B-B′ and C-C′, the full examined thickness of the TMN is dominated by grain boundary migration, while on A-A′ grain boundary migration dominates between −5 and −3 km and transitions upward to subgrain rotation between −1 and 0 km (Figure 4). In addition, six samples from the TMN exhibit subgrain rotation recrystallization locally overprinting grain boundary migration microstructures (Table S1). Collectively, our observations from the TMN are similar to those of Dutta and Mukherjee (2020), who also documented grain boundary migration and subgrain rotation recrystallization. Rocks in the Tetraogal nappe exhibit grain boundary migration on B-B′ and subgrain rotation on C-C′, but no recrystallization was observed on A-A′. In the Mata nappe, subgrain rotation was observed in the basal ~0.5 and ~1.5 km of B-B′ and C-C′, respectively, and the structurally highest sample on A-A′ exhibited bulging.

7. Quartz Crystallographic Preferred Orientations

To provide information on the 3D strain field, deformation temperature, shear sense, kinematic vorticity, and the strength of fabric development, we measured the orientations of *c*-axes of recrystallized quartz from five samples from the TMN and two samples from the Mata nappe (Table 2; Figure 10). Quartz *c*-axis orientations were measured on foliation-normal, lineation-parallel thin sections using an automated crystal fabric analyzer at the University of British Columbia, Okanagan (see Supporting Information S1 for details on analytical methods).

All seven samples exhibit CPOs characteristic of deformation within a 3D strain field that approximates plane strain (Figure 10) (e.g., Bouchez et al., 1983; Lister & Hobbs, 1980; Schmid & Casey, 1986). The four

Table 1
Summary of Raman Spectroscopy of Carbonaceous Material (RSCM) Thermometry from Samples from Transects A-A′, B-B′, and C-C′

Sample	Transect	Structural height (m)	Tectonostratigraphic unit	Lithology	R1		R2		Peak temperature (°C)			*n*
					Mean	1σ	Mean	1σ	Mean	1σ	2 SEM	
6AA	A-A′	10,600	Mata nappe	Graphitic phyllite	1.206	0.125	0.651	0.021	311	19	28	15
8AA	A-A′	8,850	Mata nappe	Graphitic phyllite	1.615	0.077	0.675	0.006	325	7	26	15
9A	A-A′	6,800	Mata nappe	Graphitic micrite	1.560	0.211	0.626	0.041	370	32	32	14
10A	A-A′	3,800	Tetraogal nappe	Graphitic phyllite	1.565	0.086	0.609	0.018	392	17	27	15
11A	A-A′	1,900	Tetraogal nappe	Marble	0.671	0.158	0.451	0.045	434	19	28	15
14BA	A-A′	0	Tso Morari nappe	Graphitic marble	0.592	0.188	0.409	0.071	460	35	33	14
12AA	A-A′	−450	Tso Morari nappe	Graphitic phyllite	0.758	0.135	0.482	0.035	418	12	28	14
13BA	A-A′	−650	Tso Morari nappe	Graphitic marble	0.415	0.142	0.365	0.067	466	37	32	15
18A	A-A′	−2,850	Tso Morari nappe	Schist	0.316	0.220	0.324	0.132	481	87	50	16
119AA	A-A′	−3,300	Tso Morari nappe	Marble	0.294	0.277	0.274	0.198	526	140	70	18
100BA	A-A′	−3,350	Tso Morari nappe	Schist	0.103	0.020	0.164	0.034	595	31	29	16
20EA	A-A′	−3,450	Tso Morari nappe	Marble	0.269	0.168	0.291	0.130	505	93	53	16
23E	A-A′	−5,300	Tso Morari nappe	Schist	0.293	0.197	0.092	0.128	511	88	49	17
113A	B-B′	7,500	Mata nappe	Limestone	1.624	0.658	0.79	0.048	168	24	35	10
114A	B-B′	7,350	Mata nappe	Limestone	1.065	0.366	0.773	0.028	152	26	30	14
116A	B-B′	7,000	Mata nappe	Limestone	0.820	0.254	0.739	0.034	153	14	27	15
111A	B-B′	5,350	Mata nappe	Limestone	0.827	0.042	0.642	0.011	262	8	26	15
110A	B-B′	5,200	Mata nappe	Lime mudstone	1.152	0.163	0.696	0.020	255	19	28	15
117A	B-B′	4,700	Mata nappe	Limestone	1.431	0.238	0.617	0.038	369	27	28	16
118A	B-B′	4,050	Mata nappe	Limestone	1.750	0.231	0.674	0.019	328	28	32	13
108A	B-B′	2,000	Mata nappe	Phyllite	0.211	0.026	0.279	0.019	504	15	25	17
109A	B-B′	1,350	Mata nappe	Phyllite	0.168	0.041	0.220	0.026	554	21	29	14
107A	B-B′	900	Tetraogal nappe	Schist	0.251	0.154	0.265	0.103	528	68	44	15
106A	B-B′	400	Tetraogal nappe	Schist	0.146	0.027	0.211	0.035	557	32	31	15
105AA	B-B′	0	Tso Morari nappe	Schist	0.166	0.049	0.229	0.050	544	39	30	18
104A	B-B′	−450	Tso Morari nappe	Quartzite	0.178	0.078	0.232	0.088	543	73	46	15
103B	B-B′	−850	Tso Morari nappe	Schist	0.206	0.095	0.255	0.086	527	66	44	14
102BA	B-B′	−1,450	Tso Morari nappe	Schist	0.179	0.073	0.239	0.076	537	61	39	16
42A	C-C′	2,100	Mata nappe	Micaceous quartzite	0.326	0.098	0.323	0.067	488	47	38	13
41A	C-C′	1950	Mata nappe	Schist	0.446	0.165	0.402	0.082	433	56	50	9
43BA	C-C′	1,350	Mata nappe	Graphitic phyllite	0.475	0.137	0.385	0.085	460	64	45	13
44A	C-C′	900	Mata nappe	Graphitic phyllite	0.541	0.059	0.397	0.045	464	38	38	11
45BA	C-C′	500	Mata nappe	Calcareous slate	0.600	0.177	0.453	0.069	415	43	34	15
46A	C-C′	50	Tetraogal nappe	Marble	0.387	0.072	0.37	0.041	454	28	30	15
47A	C-C′	0	Tso Morari nappe	Schist	0.344	0.116	0.288	0.070	530	46	43	10
48A	C-C′	−350	Tso Morari nappe	Schist	0.227	0.077	0.282	0.060	504	43	40	11

Note. R1, R2, and peak temperature values calculated using the calibration of Rahl et al. (2005). Internal variability in R1, R2, and peak temperature is indicated by 1σ uncertainty. Temperature is also reported with 2 standard errors of the mean (SEM), calculated from quadratic addition of 1σ internal error and external error of ±50°C from the Rahl et al. (2005) calibration, divided by the square root of the number of analyses (*n*).

structurally lowest samples from the TMN, which are distributed between −3,450 and −1,450 m, yielded well-defined single girdles (sample 20FA) or type-I crossed girdles (Samples 27AA, 35AA, and 102AA). Sample 14AA at the top of the TMN (0 m) yielded a weakly developed type-II crossed girdle, and samples 109A and 43A from the Mata nappe (both at 1,350 m) yielded weakly developed CPOs.

The opening angles exhibited by the four samples that yielded crossed girdles can be used to estimate the deformation temperature during the final stages of dynamic recrystallization (assuming a constant strain rate and negligible hydrolytic weakening; e.g., Kruhl, 1998; Law, 2014; Morgan & Law, 2004). Samples 27AA, 35AA, 102AA, and 14AA yielded opening angles of 67°, 44°, 55°, and 57°, respectively (Table 2; Figure 10; see Supporting Information S1 for supporting graphs), determined following the approach of Hunter et al. (2018). Using the pressure-independent calibration of Faleiros et al. (2016) (their equation 3), these opening angles correspond to deformation temperatures of 535 ± 50°C, 332 ± 50°C, 440 ± 50°C, and 457 ± 50°C. These opening angle temperatures overlap with those obtained from the TMN by Dutta and Mukherjee (2020), which generally range between ~400 ± 50°C and ~650 ± 50°C.

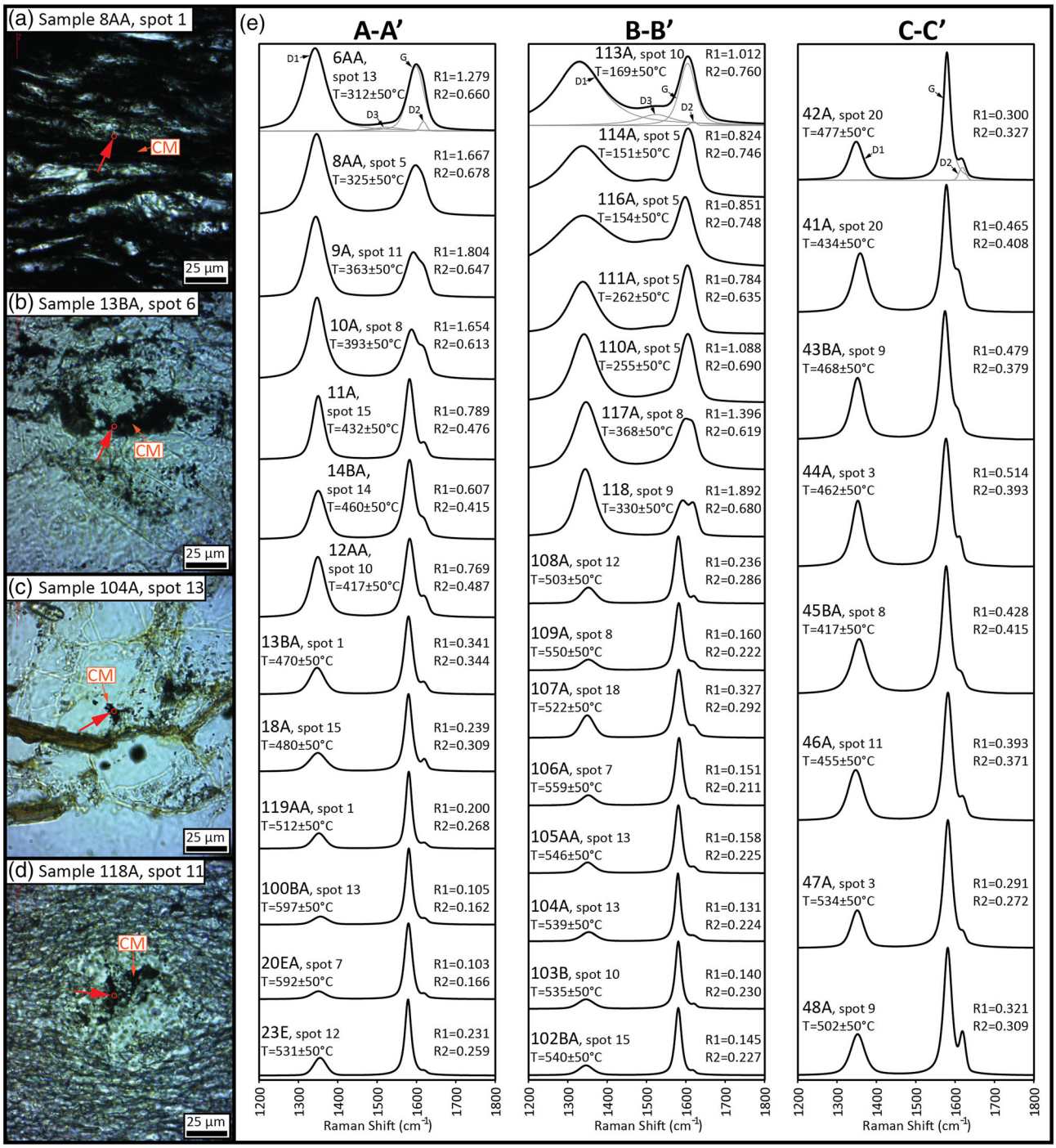

Figure 8. (a–d) Photomicrographs of representative examples of analyzed (a) laminations and (b–d) patches of carbonaceous material (CM) (taken in plane-polarized light; the red circle represents the analyzed spot; sample numbers are referenced to Figures 2–4). (e) Examples of representative Raman spectra from single spot analyses of each sample from the three transects. Samples are listed in order of increasing structural height and are referenced to Figures 2–4. Positions of the graphite band (*G*) and defect bands (D1, D2, and D3) are labeled for the top sample in each column. Peak temperatures (*T*) and R1 and R2 parameters are calculated after Rahl et al. (2005). Single spot analyses are listed with errors of ±50°C, which is the external uncertainty from the Rahl et al. (2005) calibration.

The asymmetry of *c*-axis fabric patterns allows for interpretation of shear sense from all seven samples. The five samples from the TMN exhibit CPOs with central portions that are inclined to the east relative to foliation, defining a top-to-east shear sense (Figure 10). The samples from the Mata nappe exhibit asymmetric CPOs that define top-to-south (Sample 109A) and top-to-southwest (Sample 43A) senses of shear.

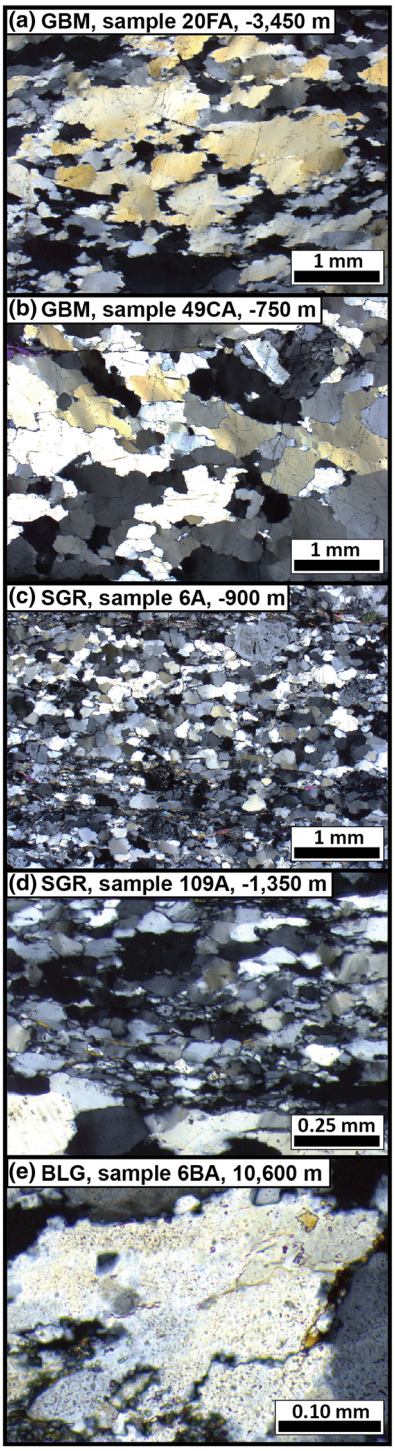

Figure 9. Photomicrographs illustrating representative quartz recrystallization microstructures (taken in cross-polarized light). (a and b) Grain boundary migration (GBM) microstructures, characterized by interfingering amoeboid quartz grains up to ~0.5–1.5 mm in diameter. (c and d) Subgrain rotation (SGR) microstructures, characterized by an equigranular texture of ~0.05- to 0.1-mm diameter, recrystallized quartz subgrains. (e) Bulging (BLG) recrystallization, as defined by localized ≤0.05-mm diameter bulges and subgrains developed along the boundaries of adjacent relict (i.e., detrital) quartz clasts.

Assuming the simplified case of steady-state plane strain (e.g., Fossen & Tikoff, 1993; Johnson et al., 2009), quartz *c*-axis fabrics can be used to quantify the kinematic vorticity number (W_n), which is interpreted to record the degree of noncoaxiality during the latest stages of shearing (e.g., Johnson et al., 2009; Wallis, 1992). W_n is a unitless ratio between 0 and 1 that quantifies the relative contributions of pure and simple shear (e.g., Means, 1994; Means et al., 1980; Passchier, 1987), with equal contributions at 0.71 (Law et al., 2004). We used the "oblique quartz shape preferred orientation" method of Wallis (1992, 1995) to calculate W_n, which utilizes the angle between foliation and the line normal to the central girdle segment of a quartz *c*-axis fabric (β) combined with the maximum elongation angle of recrystallized quartz grains measured relative to foliation (θ'_{ISA1}) (additional details on methods are in the Supporting Information S1). Because oblique grain shape preferred orientations are often interpreted record the incremental strain field during the final stages of crystal-plastic deformation (e.g., Johnson et al., 2009; Law, 2010; Xypolias, 2009, 2010), we interpret that the W_n values that we obtained from this technique give information about vorticity during late-stage shearing along the exhumation path (e.g., Law, 2010, 2014). We measured β and θ'_{ISA1} angles for five of the seven samples (20FA did not exhibit an oblique quartz grain shape fabric, and 14AA exhibited a type-II crossed girdle, which is not applicable for this method), which yielded W_n values that range from 0.90 to 0.99 (Table 2; Figure 10). These values indicate a dominant simple shear component (70–90%).

Parameters that quantify the strength (i.e., nonrandomness) of quartz fabric development have been used as proxies for relative finite strain magnitude in several recent studies to investigate strain patterns across major Himalayan shear zones (Hunter et al., 2015, 2018; Larson, 2018; Larson et al., 2017; Long et al., 2019; Starnes et al., 2020). We calculated the cylindricity index (*B*) from our seven CPO samples, which is a unitless value between 0, which represents a completely random fabric, and 1, which represents a completely nonrandom fabric (Vollmer, 1990). *B* represents the sum of the point (*P*) and girdle (*G*) end-member fabric components (Barth et al., 2010; Mainprice et al., 2015; Vollmer, 1990). *P*, *G*, random (*R*), and *B* values were calculated for each sample using the program Orient (Table 2; Figures 10 and 11). *B* values from the structurally lowest four samples of the TMN range between 0.65 and 0.97, defining strong CPO development between −3,450 and −1,450 m (Figure 11a). These are similar to cylindricity values obtained by Dutta and Mukherjee (2020) from TMN samples collected along our A-A′ and C-C′ transects, which typically range between ~0.5 and ~0.8. Moving structurally upward, *B* values at the upper boundary of the TMN (0 m) and in the overlying Mata nappe (1,350 m) decrease significantly to 0.25–0.31, indicating a decrease in CPO strength.

Following the recommendation of Mainprice et al. (2015), we also calculated CPO strength as the L2 norm of the spherical density distribution (e.g., Kilian & Heilbronner, 2017; Marti et al., 2018) using the FabricPlotR scripts (Larson, 2020) for the open-source R software environment. The density norm ranges between 1 for a homogeneous distribution and infinity for a single point distribution (Mainprice et al., 2015). The structurally lowest four samples (−3,450 to −1,450 m) have density norms (kernel half-width = 9) between 1.74 and 2.86, while the structurally highest three samples (0–1,350 m) yielded significantly lower values of

Table 2
Summary of Parameters for Determination of Deformation Temperature, Kinematic Vorticity, and Fabric Strength from Quartz Fabric Samples

Sample	Transect	Tectonostratigraphic unit	Lithology	Foliation (d, dd)[a]	Lineation (tr, pl)[b]	Thin section orientation (d, dd)[a]	Structural height relative to top of Tso Morari nappe (m)	Quartz *c-axis* opening angle	Opening angle deformation temperature (°C)[a]
43A	C-C′	Mata nappe	Quartz vein	20, 250	16, 212	78, 128	1,350	—	—
109A	B-B′	Mata nappe	Quartzite	62, 225	22, 145	37, 094	1,350	—	—
14AA	A-A′	Tso Morari nappe	Calcareous quartzite	28, 230	22, 274	74, 357	0	57°	457 ± 50°C
102AA	B-B′	Tso Morari nappe	Quartz vein	19, 100	6, 290	70, 201	−1,450	55°	440 ± 50°C
35AA	B-B′	Tso Morari nappe	Quartz vein	24, 008	16, 318	69, 231	−2,350	44°	332 ± 50°C
27AA	A-A′	Tso Morari nappe	Quartz vein	8, 030	3, 110	82, 202	−2,850	67°	535 ± 50°C
20FA	A-A′	Tso Morari nappe	Quartzite	19, 145	11, 083	76, 357	−3,450	—	—

Note. β = acute angle between foliation and line normal to central axis of single or crossed girdle in quartz c-axis pole plot (after Law et al., 2013). θ'_{ISA1} = acute angle between foliation and mean angle of long axes of recrystallized quartz clasts (after Johnson et al., 2009). W_n = kinematic vorticity number for the final stages of shearing; approximates the degree of con-coaxiality of the latest instantaneous strain ellipse (e.g., Wallis (1992).
Abbreviations: SPO = shape-preferred orientation; SE = standard error; end-member fabric components (Vollmer, 1990): P = point; G = girdle; R = random; B = cylindricity index (B = P + G). [a]Opening angle temperatures calculated from equation 3 of Faleiros et al. (2016). Temperatures are reported with ±50° C error (Kruhl, 1998). [b]Calculated using the equation $W_n = \sin(2 * (\beta + \theta'_{ISA1}))$ from Wallis (1992, 1995). [c]Percent pure shear values were determined from Law et al. (2004) and are rounded to the nearest 5%.

1.14–1.21 (Table 1). The density norm values, therefore, define a similar overall pattern to the cylindricity values (Figure 11c).

8. Finite Strain Data

Several thin sections of metasedimentary rocks from the TMN and most thin sections from the Tetraogal and Mata nappes contain elongated quartz grains that are isolated within a matrix of mica or calcite (Figures 12a–12c). These are interpreted as stretched detrital quartz clasts that represent deformed markers from which finite strain can be measured (e.g., Larson & Godin, 2009; Law et al., 2004; Long et al., 2017, 2019). In order to quantify the magnitude and orientation of 3D finite strain, we performed the Rf-ϕ method (e.g., Dunnet, 1969; Ramsay, 1967) on quartz clasts from 34 total samples of metasedimentary rocks that span all three transects (15 samples from the TMN, five from the Tetraogal nappe, and 14 from the Mata nappe).

Two foliation-normal thin sections were cut from each sample, one parallel (thin sections that end with "A") and one normal (thin sections that end with "B") to mineral stretching lineation, which are interpreted to approximate the *XZ* and *YZ* strain planes, respectively. Finite strain data are summarized in Table 3, 2D strain ellipses determined from each thin section are plotted on Figure 12d (see Supporting Information S1 for supporting data). For all samples, the 2D strain ratio (Rs) in the lineation-parallel thin section was greater than Rs in the lineation-normal thin section, and the shortening direction was subnormal to foliation. This supports the use of mesoscopic foliation and lineation to approximate the principal strain directions. Quartz clasts often exhibit lower elongation magnitudes than the surrounding mica-rich matrix (e.g., Treagus & Treagus, 2002; Tullis & Wenk, 1994; Yonkee et al., 2013); therefore, we interpret that the strain magnitudes that we measured likely represent minima.

The finite strain data show an overall decrease in strain magnitude with increasing structural level (Figure 12d). Samples from the TMN distributed between −5 and −1 km (n = 9) yielded uniformly high strain magnitudes, with $Rs_{[X/Z]}$ and $Rs_{[Y/Z]}$ values that range from 3.4 to 5.2 (average 3.9) and 2.3 to 2.6 (average 2.5), respectively. TMN samples between −1 and 0 km (n = 6) exhibit heterogeneous strain magnitudes, with $Rs_{[X/Z]}$ ranging from 2.1 to 4.7 (average 3.4) and $Rs_{[Y/Z]}$ ranging from 1.7 to 2.7 (average 2.2). Above this, samples from the Tetraogal and Mata nappes distributed between 0 and 2 km (n = 11) yielded variable but overall lower strain magnitudes, with $Rs_{[X/Z]}$ and $Rs_{[Y/Z]}$ values that range from 1.7 to 3.2 (average of 2.5) and 1.3 to 2.4 (average of 1.9), respectively. Finally, samples from the Tetraogal and Mata nappes distributed between 2 and 11 km (n = 8) exhibit uniformly low strain magnitudes, with $Rs_{[X/Z]}$

Table 2
Continued

Sample	Shear sense defined by *c*-axis pattern	β (°)	θ'_{ISA1} (°)	W_n from oblique quartz SPO method[b]	Percentage of simple shear from quartz SPO method[c]	Quartz *c*-axis fabric components			Cylindricity	Density
						P	*G*	*R*	Index (*B*)	Norm (DN)
43A	Top-to-southwest	19°	23°	0.99	90%	0.17	0.09	0.75	0.25	1.21
109A	Top-to-south	6°	33°	0.98	85%	0.07	0.22	0.71	0.29	1.14
14AA	Top-to-east	4°	—	—	—	0.02	0.29	0.69	0.31	1.17
102AA	Top-to-east	6°	34°	0.98	85%	0.25	0.40	0.35	0.65	1.94
35AA	Top-to-east	6°	26°	0.90	70%	0.18	0.54	0.28	0.72	1.74
27AA	Top-to-east	13°	26°	0.98	85%	0.28	0.44	0.29	0.71	2.02
20FA	Top-to-east	22°	—	—	—	0.20	0.77	0.03	0.97	2.86

Note. β = acute angle between foliation and line normal to central axis of single or crossed girdle in quartz c-axis pole plot (after Law et al., 2013). θ'_{ISA1} = acute angle between foliation and mean angle of long axes of recrystallized quartz clasts (after Johnson et al., 2009). W_n = kinematic vorticity number for the final stages of shearing; approximates the degree of con-coaxiality of the latest instantaneous strain ellipse (e.g., Wallis (1992).
Abbreviations: SPO = shape-preferred orientation; SE = standard error; end-member fabric components (Vollmer, 1990): P = point; G = girdle; R = random; B = cylindricity index (B = P + G).
[a]Opening angle temperatures calculated from equation 3 of Faleiros et al. (2016). Temperatures are reported with ±50°C error (Kruhl, 1998). [b]Calculated using the equation $W_n = \sin(2 * (\beta + \theta'_{ISA1}))$ from Wallis (1992, 1995). [c]Percent pure shear values were determined from Law et al. (2004) and are rounded to the nearest 5%.

ranging from 1.3 to 2.1 (average of 1.8) and $Rs_{[Y/Z]}$ ranging from 1.1 to 2.0 (average of 1.5). In summary, the data define uniformly high strain ($Rs_{[X/Z]}$ = ~3.9) within the basal 4 km of the TMN, an upward-decreasing strain gradient distributed between 1 km below and 2 km above the top of the TMN, and uniformly low strain ($Rs_{[X/Z]}$ = ~1.8) at all examined structural levels above this. The uniformly high strain distributed through the TMN that we document is also supported by Dutta and Mukherjee (2020), who argued for a lack of variation in deformation intensity with structural height within the TMN, on the basis of distributed high-cylindricity quartz fabrics and quartz grain aspect ratio statistics.

On a Flinn diagram (Figure 13a), 32 of the 34 strain ellipsoids plot in the field of apparent flattening, with two samples from the Mata nappe that plot in the field of apparent constriction. ϕ angles were measured relative to foliation and are therefore equivalent to the parameter θ′ of Ramsay and Huber (1983) (from this point on, ϕ is referred to as θ′). For samples from the TMN, θ′ was listed as positive if the grain long axis was inclined toward the west relative to foliation (consistent with a top-to-the-east shear sense) and negative if inclined toward the east (Figure 13b). For samples from the Tetraogal and Mata nappes, θ′ was listed as positive if the grain long axis was inclined toward the north, northeast, or northwest relative to foliation (consistent with a top-to-the-south, southwest, or southeast shear sense). All thin sections yielded mean θ′ values between 0° and ±10° (with one outlier of −14°) (Figure 13b). The results of the Flinn diagram combined with the low mean θ′ values indicate that nearly all samples experienced layer-normal flattening strain (e.g., Long et al., 2011, 2017).

We calculated mean kinematic vorticity numbers (W_m) for the lineation-parallel thin sections by comparing our finite strain data to W_m contours on a graph of Rs versus θ′ (Figure 10b) (referred to here as the Rs-θ′ method; e.g., Tikoff & Fossen, 1995). This method involves assuming that the orientation of mesoscopic foliation is subparallel to the boundaries of first-order shear zones, which is supported by mapping (Buchs & Epard, 2019; Epard & Steck, 2008; Steck et al., 1998; this study) that shows that the shear zones bounding the bottom and top of the Tetraogal nappe are oriented subparallel to mesoscopic foliation for a NW-SE distance of >100 km and a NE-SW distance of >40 km (Figures 1 and 2; see Supporting Information S1 for further discussion). This method also assumes that quartz clasts were homogeneously elongated in the direction of maximum finite stretching, which is supported by low standard error values for Rs (typically ±0.1–0.3) and θ′ (typically ±1–2°) for our analyzed thin sections. The idealized case of plane strain was assumed for estimation of W_m (e.g., Fossen & Tikoff, 1993; Johnson et al., 2009). However, because nearly all of the samples experienced flattening strain, the W_m values that we estimate likely represent maxima. Across the range of strain magnitudes that our samples yielded (a total Rs range of 1.1–5.2), the overestimation of W_m likely does not exceed ~0.05 (Tikoff & Fossen, 1995). The range of W_m values reported for each sample was estimated from the ±1 standard error range of mean θ′ values (Figure 13b; Table 3), and all of

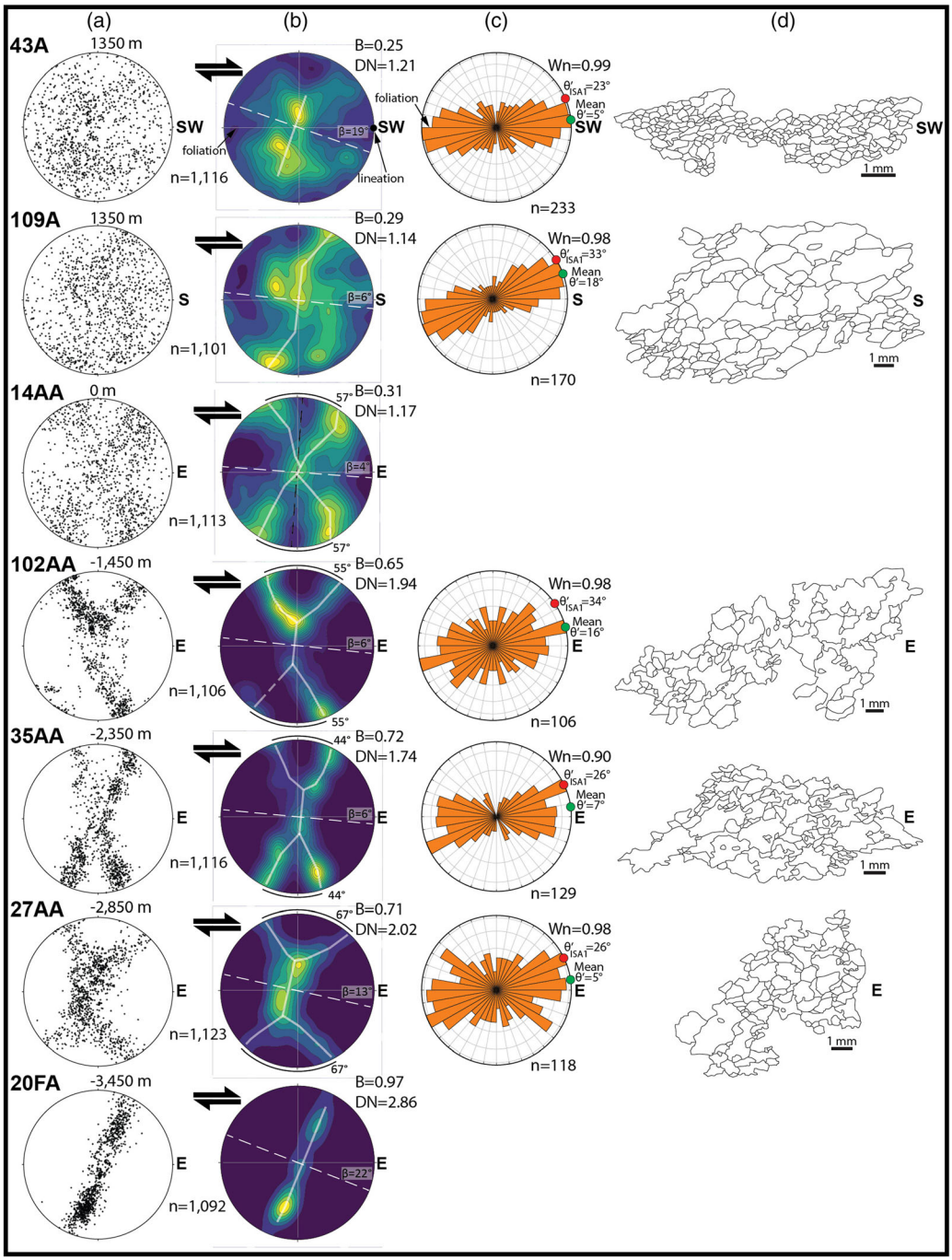

Figure 10. (a and b) Quartz *c*-axis orientations plotted on equal area stereoplots (generated using the custom R scripts of Larson, 2020), ordered by increasing structural height. Plots are oriented with foliation as a vertical plane and lineation as a horizontal line (see Sample 43A). Column (a) shows individual *c*-axes, and Column (b) shows pole figures (contoured relative to multiples of a random distribution) with visually interpreted fabric skeletons (e.g., Lister & Williams, 1979). The number of *c*-axes measured (*n*), fabric opening angles, β angles, interpreted shear sense, cylindricity values (*B*), and density norm (DN) values are shown for each sample. (c) Rose diagrams (generated using Orient) graphing θ′ measurements (i.e., the angle between the long axis of a recrystallized quartz grain and foliation; e.g., Ramsay & Huber, 1983) of the quartz grains outlined in Column D, which were used to determine the θ'_{ISA1} angle (the maximum value of a coherent population of θ′ measurements; see Supporting Information S1 for supporting data). Rose diagrams are oriented the same as the stereoplots in (a) and (b). Kinematic vorticity (W_n) ranges calculated from the equation $W_n = \sin(2(\beta + \theta'_{ISA1}))$ (Wallis, 1992, 1995) are shown for all samples except 20FA, which did not exhibit an oblique grain shape fabric, and 14AA, which yielded a type-II crossed girdle and is therefore not applicable for this method. (d) Digitized areas of the thin sections that illustrate the oblique quartz grain shape-preferred orientation for five samples, which were used for measuring θ'_{ISA1} values (see Supporting Information S1 for supporting data). Quartz grains are outlined in black and contain white fill, and all other mineral phases are filled in black. The diagrams are oriented with foliation as horizontal and structural-up toward the top of the page.

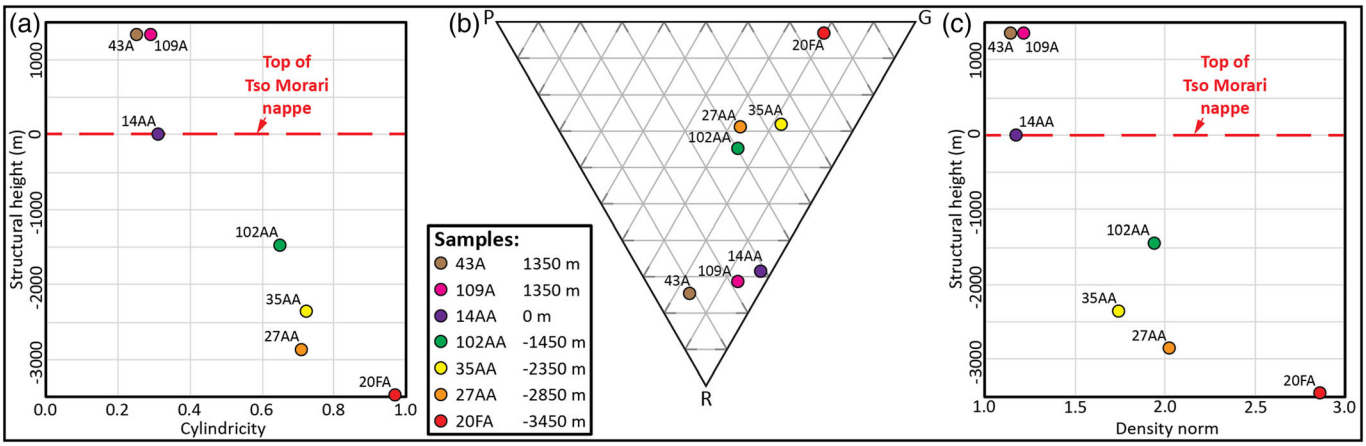

Figure 11. (a) Graph of cylindricity values obtained from the quartz *c*-axis fabric samples versus structural height relative to the top of the TMN. (b) Ternary diagram showing point (*P*), girdle (*G*), and random (*R*) end-member fabric components (e.g., Vollmer, 1990) from the quartz *c*-axis fabric samples. Generated using Orient. (c) Graph of density norm values obtained from the fabric samples versus structural height relative to the top of the TMN.

our W_m values are rounded to the nearest 0.05. Twenty-nine of the 34 total samples yielded W_m values that ranged between 0.00 and 0.45 (70–100% pure shear), with four samples that yielded values as high as 0.50–0.55 (as little as 60–65% pure shear), and one outlier that yielded a value as high as 0.70 (as little as 50% pure shear).

To quantify trends in finite strain with structural height, we calculated the percent elongation in the lineation-parallel (*X*) and lineation-normal (*Y*) directions, as well as percent shortening subnormal to foliation (*Z*) (Table 3). These quantities were calculated by comparing the lengths of the *X*, *Y*, and *Z* directions of the 3D strain ellipsoid for each sample to the diameter of a sphere with the same volume (e.g., Ramsay, 1967). In addition, using methods outlined in Law (2010) and Xypolias et al. (2010), strain magnitudes and W_m values were integrated to calculate transport-parallel lengthening and transport-parallel shortening for individual strain samples (see the Supporting Information S1 for details on methods) (Table 3; Figures 13c and 13d). Both transport-parallel lengthening and transport-normal shortening decrease moving structurally upward. Between −5 and −1 km, the TMN yielded an average lengthening of 63 ± 8% (1 standard error) and an average shortening of 46 ± 2%. Between −1 and 0 km, the TMN exhibits an average lengthening of 54 ± 9% and an average shortening of 41 ± 3%. The basal 2 km of the Tetraogal and Mata nappes yielded average lengthening and shortening values of 33 ± 5% and 32 ± 3%, respectively. Between 2 and 11 km above the top of the TMN, the Tetraogal and Mata nappes exhibit an average lengthening of 14 ± 2% and an average shortening of 18 ± 3%. In summary, the data define a trend of high-magnitude lengthening and shortening in the lowest 4 km of the TMN that decrease upward by a factor of 4.5 (lengthening) and by a factor of 2.6 (shortening) by a height of 2 km above the top of the TMN (Figures 13c and 13d). The intervening 3-km-thick interval defines a significant upward-decreasing strain gradient. In contrast, lineation-normal (*Y*) elongation exhibits less variability, and decreases upward from 16 ± 2% in the lowest 4 km of the TMN, to 13 ± 2% between 1 km below and 2 km above the top of the TMN, to 10 ± 3% between 2 and 11 km above (Figure 13e).

The mean elongation direction of quartz clasts in lineation-parallel thin sections, as denoted by the sign of θ′, can be used to determine shear sense for individual samples (e.g., Passchier & Trouw, 2005; Ramsay, 1967). Under the sign convention that we used for samples from the TMN, a positive mean θ′ value corresponds to a top-to-east shear sense, and negative corresponds to top-to-west (Figure 13b). For samples from the Tetraogal and Mata nappes, a positive mean θ′ value corresponds to a southward component of shear (top-to-south, southwest, or southeast), and negative corresponds to a northward component (top-to-north, northwest, or northeast). Twenty-five of the 34 total samples exhibited mean θ′ values that were ≤±4°, with error ranges that often overlap with or lie within 1–2° of foliation. We did not interpret these samples to represent robust shear-sense indicators. However, we did interpret shear sense for the remaining nine samples that yielded mean θ′ values that were ≥±5° (Figures 4 and 13b; Table 3). These included one sample

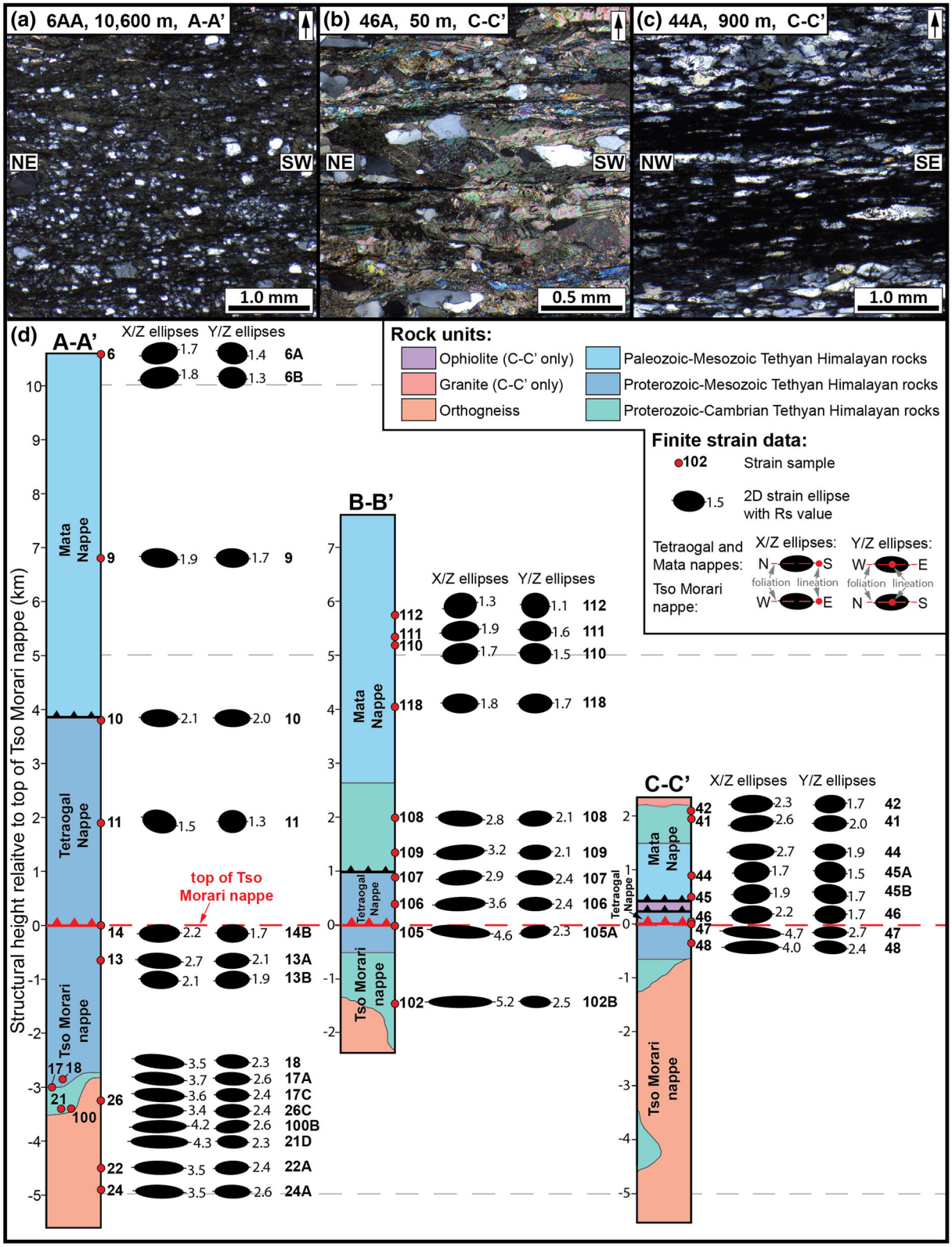

Figure 12. (a–c) Photomicrographs of representative examples of elongated detrital quartz clasts isolated within a matrix of (a and c) mica or (b) calcite, which were utilized for finite strain analyses (cross-polarized light; foliation is horizontal and arrow points toward structural-up). (d) Simplified tectonostratigraphic columns of the three transects, with 2D finite strain ellipses shown (the *X*/*Z* ellipses are from lineation-parallel thin sections and the *Y*/*Z* ellipses are from lineation-normal thin sections). Strain ellipses are scaled to constant volume.

Tectonics

10.1029/2020TC006482

Table 3
Summary of Finite Strain Data, Mean Kinematic Vorticity Values, Shear Sense, and Lengthening and Shortening Magnitudes from Strain Samples

Thin section	Transect	Tectonostratigraphic unit	Lithology	Structural height relative to top of Tso Morari nappe (m)	Foliation (d, dd)	Lineation (tr, pl)	Crenulation cleavage axis (tr, pl)	Orientation of thin section relative to lineation or crenulation
6AA	A-A′	Mata nappe	Graphitic phyllite	10,600	82, 230	82, 230	—	Parallel to lineation
6AB								Normal to lineation
6BA	A-A′	Mata nappe	Micaceous quartzite	10,600	74, 245	-—	39, 324	Normal to crenulation
6BB								Parallel to crenulation
9A	A-A′	Mata nappe	Graphitic micrite	6,800	62, 040	—	7, 126	Normal to crenulation
9B								Parallel to crenulation
10A	A-A′	Tetraogal nappe	Graphitic phyllite	3,800	88, 035	—	10, 307	Normal to crenulation
10B								Parallel to crenulation
11A	A-A′	Tetraogal nappe	Marble	1900	72, 010	—	18, 288	Normal to crenulation
11B								Parallel to crenulation
14BA	A-A′	Tso Morari nappe	Graphitic marble	0	19, 219	16, 256	—	Parallel to lineation
14BB								Normal to lineation
13AA	A-A′	Tso Morari nappe	Micaceous marble	−650	32, 235	30, 264	—	Parallel to lineation
13AB								Normal to lineation
13BA	A-A′	Tso Morari nappe	Graphitic marble	−650	34, 235	26, 282	—	Parallel to lineation
13BB								Normal to lineation
18A	A-A′	Tso Morari nappe	schist	−2,850	3, 130	3, 110	—	Parallel to lineation
18B								Normal to lineation
17AA	A-A′	Tso Morari nappe	Micaceous quartzite	−3,000	31, 055	24, 094	—	Parallel to lineation
17AB								Normal to lineation
17CA	A-A′	Tso Morari nappe	Schist	−3,000	26,190	5, 106	—	Parallel to lineation
17CB								Normal to lineation
26CA	A-A′	Tso Morari nappe	Schist	−3,250	10, 025	3, 109	—	Parallel to lineation
26CB								Normal to lineation
100BA	A-A′	Tso Morari nappe	Schist	−3,350	1, 200	1, 220	—	Parallel to lineation
100BB								Normal to lineation
21DA	A-A′	Tso Morari nappe	Schist	−3,400	29, 020	6, 101	—	Parallel to lineation
21DB								Normal to lineation
22AA	A-A′	Tso Morari nappe	Schist	−4,500	26, 060	—	—	Parallel to local lineation
22AB								Normal to local lineation
24AA	A-A′	Tso Morari nappe	schist	−4,900	18, 305	—	—	Parallel to local lineation
24AB								Normal to local lineation
112A	B-B′	Mata nappe	Limestone	5,750	20, 260	12, 312	—	Parallel to lineation
112B								Normal to lineation
111A	B-B′	Mata nappe	limestone	5,350	37, 240	—	—	Parallel to dip direction
111B								Parallel to strike direction
110A	B-B′	Mata nappe	Lime mudstone	5,200	22, 260	—	—	Normal to local crenulation
110B								Parallel to local crenulation
118A	B-B′	Mata nappe	Limestone	4,050	11, 240	—	—	Parallel to dip direction

Tectonics

10.1029/2020TC006482

Table 3
Continued

Thin section	Transect	Tectonostratigraphic unit	Lithology	Structural height relative to top of Tso Morari nappe (m)	Foliation (d, dd)	Lineation (tr, pl)	Crenulation cleavage axis (tr, pl)	Orientation of thin section relative to lineation or crenulation
118B								Parallel to strike direction
108A	B-B′	Mata nappe	Phyllite	2000	33, 230	3, 316	—	Parallel to lineation
108B								Normal to lineation
109A	B-B′	Mata nappe	Micaceous quartzite	1,350	62, 225	22, 145	—	Parallel to lineation
109B								Normal to lineation
107A	B-B′	Tetraogal nappe	Schist	900	35, 255	8, 332	—	Parallel to lineation
107B								Normal to lineation
106A	B-B′	Tetraogal nappe	Schist	400	13, 250	8, 306	—	Parallel to lineation
106B								Normal to lineation
105AA	B-B′	Tso Morari nappe	Schist	0	11, 265	10, 300	—	Parallel to lineation
105AB								Normal to lineation
102BA	B-B′	Tso Morari nappe	Schist	−1,450	30, 115	26, 141	—	Parallel to lineation
102BB								Normal to lineation
42A	C-C′	Mata nappe	Micaceous quartzite	2,100	32, 235	14, 172	—	Parallel to lineation
42B								Normal to lineation
41A	C-C′	Mata nappe	Schist	1950	28, 160	20, 203	—	Parallel to lineation
41B								Normal to lineation
44A	C-C′	Mata nappe	Graphitic phyllite	900	28, 125	—	17, 067	Normal to crenulation
44B								Parallel to crenulation
45AA	C-C′	Mata nappe	calcareous quartzite	500	32, 155	30, 172	—	Parallel to lineation
45AB								Normal to lineation
45BA	C-C′	Mata nappe	Calcareous slate	500	34, 155	34, 155	—	Parallel to lineation
45BB								Normal to lineation
46A	C-C′	Tetraogal nappe	Marble	50	29, 135	28, 146	—	Parallel to lineation
46B								Normal to lineation
47A	C-C′	Tso Morari nappe	Schist	0	9, 155	9, 116	—	Parallel to lineation
47B								Normal to lineation
48A	C-C′	Tso Morari nappe	Schist	−350	35, 240	28, 210	—	Parallel to lineation
48B								Normal to lineation

Note. Rs = tectonic elongation (long axis to short axis ratio); φ = angle between long axis and foliation (equal to θ′ of Ramsay & Huber, 1983; see text for discussion of sign conventions). W_m = mean kinematic vorticity number.
Abbreviations: d, dd = dip, dip direction notation. tr, pl = trend, plunge notation. SE = standard error. [a]W_m (mean kinematic vorticity) values were rounded to nearest 0.05. [b]Percent pure shear values were determined from Law et al. (2004) and were rounded to nearest 5%. [c]Calculated by restoring the 3D strain ellipsoid of each sample to a sphere of the same volume and then comparing lengths before and after strain. Rounded to the nearest integer. Errors calculated from the 1 SE errors reported for each 2D strain ellipse. [d]Calculated using the equations from Fig. 10 of Law (2010) and Fig. 11 of Xypolias et al. (2010) and rounded to the nearest integer. See Supporting Information S1 for additional information on methods and supporting calculations.

Tectonics

10.1029/2020TC006482

Table 3
Continued

Thin section orientation (d, dd)	Rs (±1 SE)	φ (equal to θ′) (±1 SE)	Shear sense from Rs vs. θ′ graph	W_m range from Rs vs. θ′ method[a]	% Pure shear from Rs vs. θ′ method[b]	Lineation-parallel (*X*) elongation (%)[c]	Lineation-normal (*Y*) elongation (%)[c]	Foliation-normal (*Z*) shortening (%)[c]	Transport-parallel lengthening range (%)[d]	Transport-normal shortening range (%)[d]
90, 320	1.7 ± 0.11.7 ± 0.1	9 ± 29 ± 2	Top-to-SW	0.30–0.50	65–80%	27 ± 227 ± 2	5 ± 35 ± 3	25 ± 325 ± 3	6–17	8–19
8, 050	1.4 ± 0.11.4 ± 0.1	−10 ± 3–10 ± 3								
52, 146	1.8 ± 0.11.8 ± 0.1	7 ± 27 ± 2	Top-to-SW	0.30–0.45	70–80%	36 ± 236 ± 2	−2 ± 3–2 ± 3	25 + 4/ -3	17–29	14–21
42, 350	1.3 ± 0.11.3 ± 0.1	−5 ± 3–5 ± 3								
84, 308	1.9 ± 0.11.9 ± 0.1	−5 ± 3–5 ± 3	Top-to-NE	0.10–0.40	70–95%	29 ± 229 ± 2	15 + 3/ −2	32 + 3/ −2	11–20	19–27
30, 209	1.7 ± 0.11.7 ± 0.1	-2 ± 2–2 ± 2								
10, 292	2.1 ± 0.12.1 ± 0.1	-2 ± 1–2 ± 1	—	0.05–0.15	90–95%	30 ± 230 ± 2	24 ± 224 ± 2	38 ± 238 ± 2	18–20	30–31
80, 129	2.0 ± 0.1	−1 ± 1								
72, 104	1.5 ± 0.11.5 ± 0.1	−14 ± 4–14 ± 4	Top-to-N	0.40–0.70	50–70%	20 ± 220 ± 2	4 ± 34 ± 3	20 ± 420 ± 4	0–6	0–9
36, 248	1.3 ± 0.1	0 ± 4								
79, 342	2.2 ± 0.12.2 ± 0.1	1 ± 21 ± 2	—	0.00–0.15	90–100%	42 ± 242 ± 2	10 ± 310 ± 3	36 ± 236 ± 2	34–36	32–33
74, 076	1.7 ± 0.1	−1 ± 3								
79, 346	2.7 ± 0.2	−3 ± 1	—	0.10–0.25	80–95%	51 ± 5	18 ± 1	44 ± 2	33–39	36–39
61, 084	2.1 ± 0.1	1 ± 1								
70, 358	2.1 ± 0.1	−3 ± 2	—	0.05–0.25	80–95%	32 ± 2	20 ± 2	37 ± 2	24–30	28–31
64, 101	1.9 ± 0.1	3 ± 2								
89, 204	3.5 ± 0.2	−6 ± 1	Top-to-W	0.40–0.50	65–70%	75 ± 4	15 ± 1	50 ± 2	30–43	33–39
87, 292	2.3 ± 0.1	−4 ± 2								
74, 179	3.7 ± 0.3	−4 ± 1	—	0.25–0.40	70–80%	74 ± 7	22 ± 0	53 ± 2	37–50	40–45
75, 272	2.6 ± 0.1	−2 ± 1								
65, 020	3.6 ± 0.2	−3 ± 1	—	0.15–0.35	75–90%	75 ± 4	17 ± 1	51 ± 2	48–59	42–46
86, 288	2.4 ± 0.1	−1 ± 1								
89, 199	3.4 ± 0.2	1 ± 1	—	0.00–0.15	90–100%	69 ± 4	19 ± 1	50 ± 2	53–56	45–46
89, 290	2.4 ± 0.1	0 ± 1								
89, 310	4.2 ± 0.2	1 ± 1	—	0.00–0.20	85–100%	89 ± 4	17 ± 1	55 ± 1	71–75	50–51
89, 038	2.6 ± 0.1	6 ± 2								
61, 188	4.3 ± 0.3	−1 ± 1	—	0.00–0.20	85–100%	100 + 7/ −6	7 ± 1	53 ± 2	87–94	50–52
84, 282	2.3 ± 0.1	−2 ± 1								
76, 185	3.5 ± 0.2	−1 ± 1	—	0.00–0.15	90–100%	72 ± 4	18 ± 1	51 ± 2	58–60	46–47
71, 278	2.4 ± 0.1	2 ± 1								
80, 190	3.5 ± 0.3	−2 ± 1	—	0.05–0.25	80–95%	68 + 8/ −7	25 ± 0	52 ± 2	44–50	44–46
74, 098	2.6 ± 0.1	−1 ± 2								
75, 037	1.3 ± 0.1	10 ± 4	Top-to-SE	0.25–0.55	60–80%	15 ± 2	−2 + 4/ −3	11 ± 5	0–12	0–9
77, 134	1.1 ± 0.1	−4 ± 4								
90, 330	1.9 ± 0.1	6 ± 2	Top-to-SW	0.20–0.40	70–85%	31 ± 2	10 ± 3	31 ± 3	12–21	19–25
53, 060	1.6 ± 0.1	−5 ± 3								
70, 052	1.7 ± 0.1	8 ± 4	Top-to-SE	0.20–0.55	60–85%	24 ± 2	10 ± 3	27 ± 3	2–15	4–21
81, 148	1.5 ± 0.1	−3 ± 4								

Tectonics

10.1029/2020TC006482

Table 3
Continued

Thin section orientation (d, dd)	Rs (±1 SE)	φ (equal to θ′) (±1 SE)	Shear sense from Rs vs. θ′ graph	W_m range from Rs vs. θ′ method[a]	% Pure shear from Rs vs. θ′ method[b]	Lineation-parallel (*X*) elongation (%)[c]	Lineation-normal (*Y*) elongation (%)[c]	Foliation-normal (*Z*) shortening (%)[c]	Transport-parallel lengthening range (%)[d]	Transport-normal shortening range (%)[d]
90, 330	1.8 ± 0.1	−1 ± 3	—	0.00–0.20	85–100%	24 ± 2	17 ± 2	31 ± 3	15–16	23–25
79, 060	1.7 ± 0.1	1 ± 2								
57, 043	2.8 ± 0.1	−3 ± 2	—	0.10–0.35	75–95%	55 ± 1	16 ± 2	45 + 2/ −1	31–44	34–40
87, 138	2.1 ± 0.1	4 ± 1								
37, 094	3.2 ± 0.3	4 ± 1	—	0.20–0.35	75–85%	70 ± 8	11 ± 0	47 + 3/ -2	45–55	38–42
76, 322	2.1 ± 0.1	2 ± 2								
57, 056	2.9 ± 0.2	4 ± 2	—	0.10–0.40	70–95%	52 ± 5	26 ± 1	48 ± 2	22–36	33–41
81, 154	2.4 ± 0.1	−4 ± 2								
80, 033	3.6 ± 0.3	2 ± 1	—	0.10–0.25	80–95%	75 + 8/ −7	17 ± 0	51 ± 2	56–62	45–47
82, 127	2.4 ± 0.1	0 ± 1								
84, 028	4.6 ± 0.4	−4 ± 1	—	0.30–0.45	70–80%	110 ± 9	5 ± 0	54 ± 2	70–91	44–50
80, 121	2.3 ± 0.1	7 ± 2								
76, 228	5.2 ± 0.3	0 ± 1	—	0.00–0.10	95–100%	121 + 6/ −5	6 ± 1	57 ± 1	111–113	56
64, 322	2.5 ± 0.1	−2 ± 2								
62, 089	2.3 ± 0.12.3 ± 0.1	1 ± 21 ± 2	—	0.00–0.15	90–100%	46 ± 146 ± 1	8 ± 38 ± 3	37 ± 237 ± 2	39–41	33–34
74, 350	1.7 ± 0.1	3 ± 2								
72, 286	2.6 ± 0.12.6 ± 0.1	5 ± 15 ± 1	Top-to-S	0.25–0.35	75–85%	50 ± 150 ± 1	15 ± 215 ± 2	42 ± 242 ± 2	28–34	32–35
71, 023	2.0 ± 0.1	0 ± 2								
74, 246	2.7 ± 0.12.7 ± 0.1	1 ± 11 ± 1	—	0.00–0.10	95–100%	57 ± 157 ± 1	10 + 3/ −2	42 ± 242 ± 2	48–49	39
68, 342	1.9 ± 0.1	−1 ± 1								
81, 256	1.7 ± 0.11.7 ± 0.1	3 ± 23 ± 2	—	0.05–0.25	85–95%	24 ± 224 ± 2	10 ± 310 ± 3	27 ± 327 ± 3	13–18	20–23
61, 010	1.5 ± 0.1	−5 ± 3								
90, 245	1.9 ± 0.11.9 ± 0.1	2 ± 22 ± 2	—	0.00–0.20	85–100%	29 ± 229 ± 2	15 + 3/ −2	32 + 3/ −2	18–20	25–27
56, 335	1.7 ± 0.1	−7 ± 2								
84, 232	2.2 ± 0.22.2 ± 0.2	2 ± 22 ± 2	—	0.00–0.25	85–100%	42 ± 642 ± 6	10 ± 110 ± 1	36 ± 336 ± 3	30–36	30–33
64, 336	1.7 ± 0.1	−10 ± 2								
86, 025	4.7 ± 0.34.7 ± 0.3	−3 ± 1−3 ± 1	—	0.20–0.40	70–85%	102 ± 4,102 ± 4	16 ± 316 ± 3	57 ± 257 ± 2	63–80	47–52
83, 294	2.7 ± 0.2	0 ± 10 ± 1								
78, 130	4.0 ± 0.44.0 ± 0.4	0 ± 10 ± 1	—	0.00–0.10	95–100%	88 ± 1,088 ± 10	13 ± 013 ± 0	53 ± 253 ± 2	74–77	50
62, 030	2.4 ± 0.1	−5 ± 1								

Note. Rs = tectonic elongation (long axis to short axis ratio); φ = angle between long axis and foliation (equal to θ′ of Ramsay & Huber, 1983; see text for discussion of sign conventions). W_m = mean kinematic vorticity number.
Abbreviations: d, dd = dip, dip direction notation. tr, pl = trend, plunge notation. SE = standard error.
[a]W_m (mean kinematic vorticity) values were rounded to nearest 0.05. [b]Percent pure shear values were determined from Law et al. (2004) and were rounded to nearest 5%. [c]Calculated by restoring the 3D strain ellipsoid of each sample to a sphere of the same volume and then comparing lengths before and after strain. Rounded to the nearest integer. Errors calculated from the 1 SE errors reported for each 2D strain ellipse. [d]Calculated using the equations from Fig. 10 of Law (2010) and Fig. 11 of Xypolias et al. (2010) and rounded to the nearest integer. See Supporting Information S1 for additional information on methods and supporting calculations.

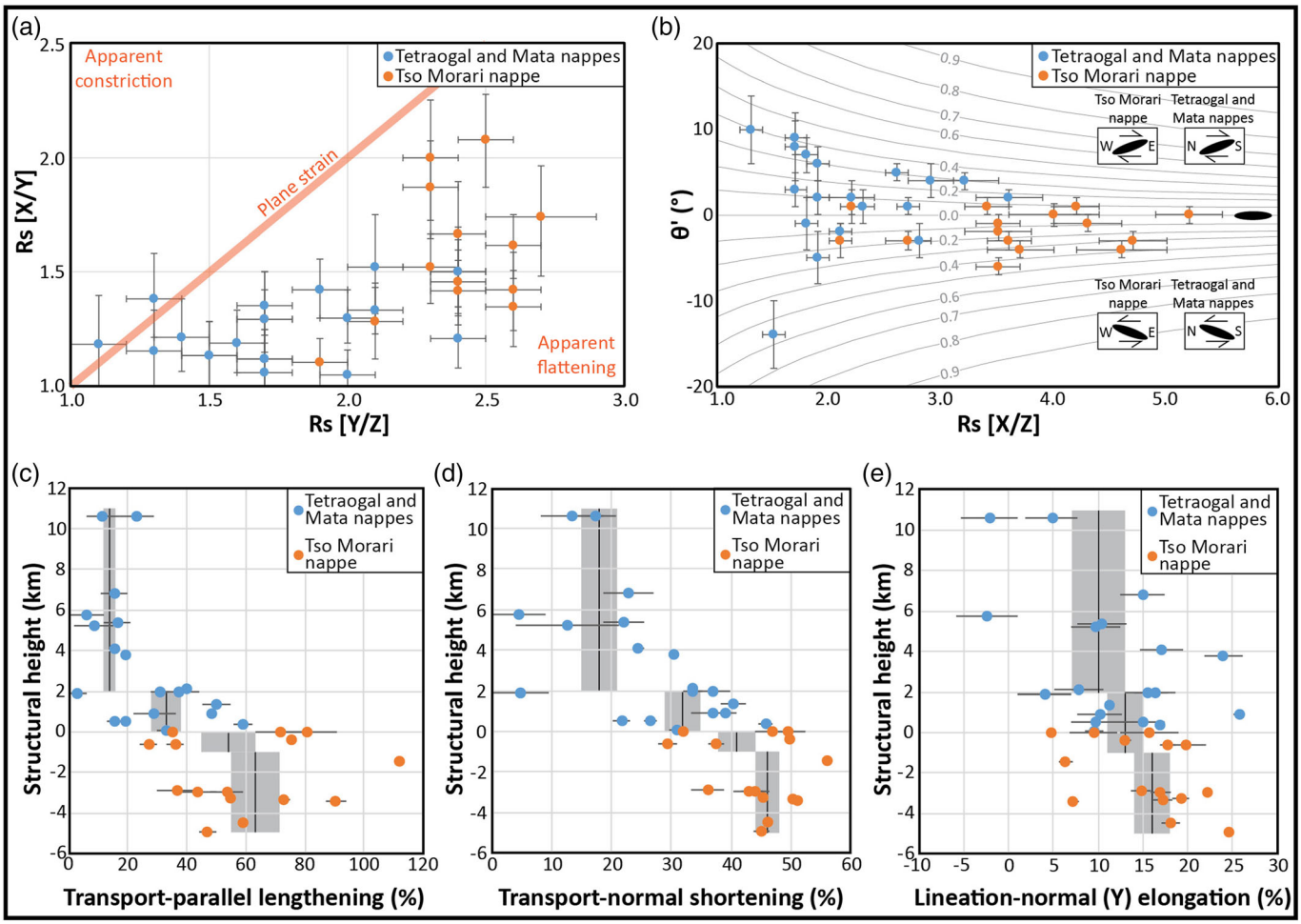

Figure 13. (a) Flinn diagram showing 3D strain fields for constant-volume deformation. Error bars are shown at the 1 standard error level. (b) Plot of tectonic strain in lineation-parallel thin sections ($Rs_{[X/Z]}$) versus the mean angle of elongation relative to foliation (θ′), with contours of mean kinematic vorticity (W_m) for plane strain deformation plotted (e.g., Tikoff & Fossen, 1995). Error bars are shown at the 1 standard error level. For samples from the TMN, a positive θ′ corresponds to a top-to-east shear sense and for samples from the Tetraogal and Mata nappes, a positive θ′ corresponds to a component of shear toward the south (including top-to-south, southeast, or southwest shear senses for different samples). (c–e) Graphs of percent transport-parallel lengthening, transport-normal shortening, and lineation-normal (*Y*) elongation versus structural height relative to the top of the TMN. Error bars for (c) and (d) are based on the range of values reported on Table 3, and error bars for (e) are based on the 1 standard error values reported for the *Y*/*Z* strain ellipse for each sample (Table 3). Gray boxes with thick black lines in the middle represent the mean value (±1 standard error) for that specific range of structural levels.

from the TMN on transect A-A′ (Sample 18), which yielded a top-to-west shear sense, one sample from the Tetraogal nappe on A-A′ (sample 11) that yielded a top-to-north shear sense, and seven total samples from the Mata nappe that span all three transects, six of which that define a top-to-south, southeast, or southwest shear sense (Samples 6A, 6B, 41, 110, 111, and 112) and one that defines a top-to-northeast shear sense (Sample 9).

9. Discussion

9.1. Ductile Strain Distribution

The data sets presented above indicate that the TMN is a >5.5-km-thick nappe that experienced intense, distributed, top-to-east ductile shearing, which can be differentiated from the lower-magnitude, south-vergent deformation observed in the overlying Tetraogal and Mata nappes. The structural data sets that distinguish the TMN (summarized on Figure 14) include the following: (1) prevalent E-W-trending stretching lineations that transition abruptly upward to more sparsely distributed, SE-, SW-, or S-trending lineations in the

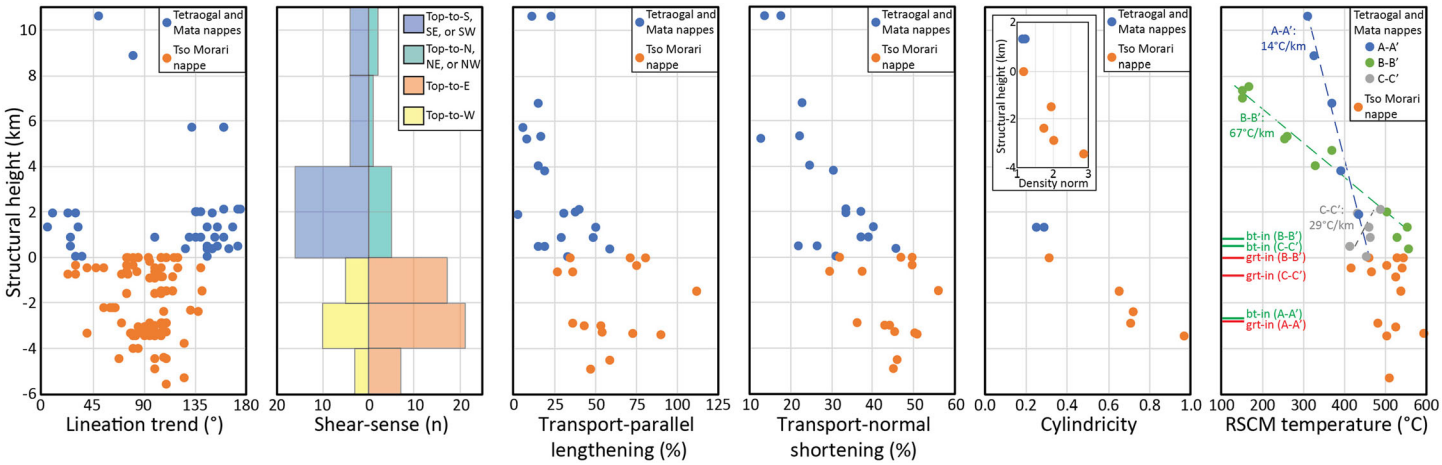

Figure 14. Graphs of structural and metamorphic data sets that characterize the TMN, including (from left to right) the trend direction of mineral stretching lineations (trend azimuths between 180° and 360° were converted into azimuths between 0° and 180°), the total number of shear-sense indicators observed, transport-parallel lengthening and transport-normal shortening (data are shown without error bars for simplicity), cylindricity values of quartz fabric samples (inset graph shows density norm values), and RSCM temperatures (data are shown without error bars for simplicity; best fit lines are shown for each transect).

overlying nappes; (2) kinematic observations that show a dominant top-to-east shear sense in the TMN that transitions upward to a dominant southward component of shearing in the overlying nappes; (3) finite strain data that define high-magnitude transport-parallel lengthening (63% average) and transport-normal shortening (46% average) in the lowest 4.5 km of the TMN, an upward-decreasing strain gradient that spans the top 1 km of the TMN and the basal 2 km of the overlying nappes, and low-magnitude lengthening (14% average) and shortening (18% average) between 2 and 11 km above the TMN (Figure 15); and (4) a trend in quartz CPO strength (which has been interpreted as a proxy for relative finite strain magnitude; e.g., Hunter et al., 2018; Larson et al., 2017) defined by cylindricity and density

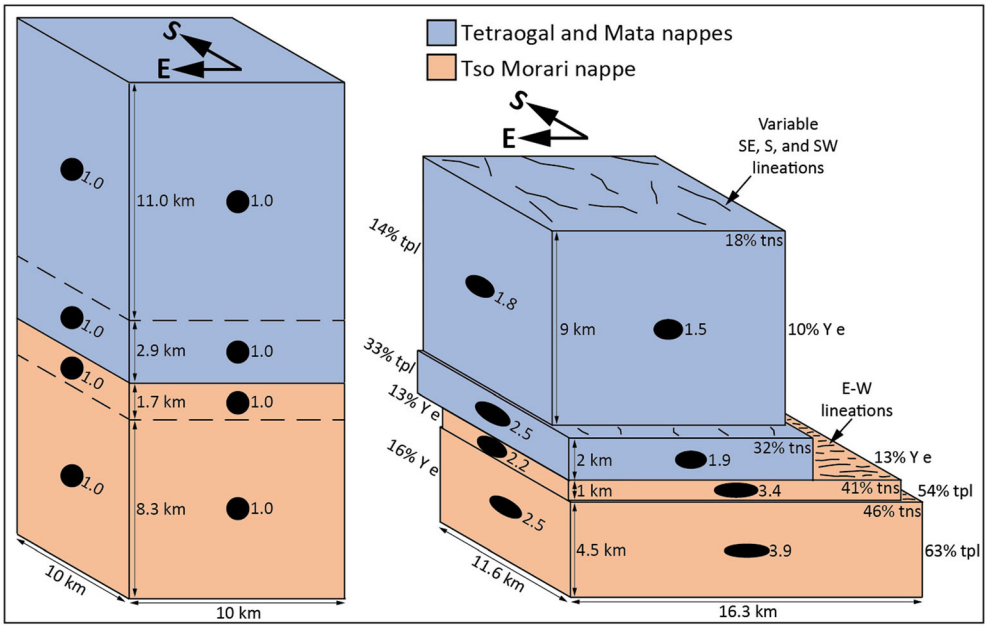

Figure 15. Diagrams illustrating the change in dimensions of a 10 km × 10 km area of the TMN and Tetraogal/Mata nappes before (left-hand diagram) and after (right-hand diagram) the measured average finite strain (tpl = transport-parallel lengthening, tns = transport-normal shortening, Y e = lineation-normal elongation). Diagrams account for distributed microscale finite strain only and do not attempt to illustrate discrete displacements on the shear zones at the base of the Mata and Tetraogal nappes.

norm values of 0.65–0.97 and 1.74–2.86, respectively, between ~3.5 and ~1.5 km below the top of the TMN, which decrease upward to 0.25–0.31 and 1.14–1.21 between ~0 and ~1.5 km above its top boundary (Figure 14).

To interpret the kinematics of shearing during extrusion of the TMN, we follow the structural model of Epard and Steck (2008) (their Fig. 20), in which the shear zones that bounded the TMN during its initial extrusion originally dipped to the northeast, and the folding of the TMN into its present-day geometry of a NW-plunging antiform (Figure 2) took place after motion on these shear zones had ceased. Differences in 3D strain geometry and kinematic vorticity yielded by the finite strain and quartz CPO analyses provide insight into the strain path of the TMN. The finite strain analyses of isolated detrital quartz grains yielded W_m values between 0.00–0.45 (70–100% pure shear), defining layer-normal flattening strain (albeit with a minor average Y elongation of 16% and a high X to Y elongation ratio of ~5:1). In contrast, the CPO-based method yielded W_n values of 0.90–0.99 (70–90% simple shear) and yielded c-axis patterns characteristic of a 3D strain field that approximates plane strain (e.g., Lister & Hobbs, 1980; Schmid & Casey, 1986). Quartz CPOs are often interpreted to reflect recrystallization that occurred during the later stages of shearing along the exhumation path (e.g., Law, 2014), which is supported by opening angle temperatures yielded by two of our fabric samples that are lower than peak RSCM temperatures (Figure 4). Therefore, we interpret that the TMN experienced a deformation path that progressed from pure shear-dominant flattening strain to simple shear-dominant, plane strain deformation, defining an accelerating strain path (e.g., Simpson & De Paor, 1993, 1997). Collectively, the strain data indicate that westward extrusion of the TMN was accompanied by significant elongation in the transport direction (i.e., "extending flow" of Price, 1972) (Figure 15).

9.2. Pressure-Temperature Evolution

Our temperature data help refine the P-T-t history of the TMN. Peak UHP metamorphism of mafic eclogites has traditionally been interpreted to have occurred at pressures of ~25–27 kbar and temperatures of ~550–650°C (de Sigoyer et al., 1997, 2000; Guillot et al., 1997; Pan et al., 2020; Sachan et al., 2004; St.-Onge et al., 2013) (Figures 16a and 16d). However, some studies have interpreted UHP conditions at higher pressures of ~44–48 kbar and temperatures of ~650–800°C (Mukherjee et al., 2003; Wilke et al., 2015). Chatterjee and Jagoutz (2015) also interpreted maximum pressure conditions of ~22–23 kbar at ~400–425°C, although this P-T condition falls outside of the coesite stability field. Our RSCM temperatures for the majority of samples analyzed from the TMN fall between ~500 and ~625°C (Figure 16a), which overlap with or are slightly lower than many prior temperature estimates at peak pressure (550 ± 50°C by Guillot et al., 1997; 580 ± 60°C by de Sigoyer et al., 1997; ~640°C by Sachan et al., 2004; 630–645°C by St.-Onge et al., 2013; 660 ± 100°C by Wilke et al., 2015; and 545–565°C by Pan et al., 2020), but are distinctly lower than estimates of ~700–800°C by Mukherjee and Sachan (2001) and Mukherjee et al. (2003). Thus, the RSCM data rule out very high temperatures of UHP metamorphism. An absence of partial melting textures in the Puga orthogneiss and interacalated metasedimentary rocks also imposes a temperature limit of ≤700°C (muscovite dehydration-melting) and possibly ≲650°C (wet melting) (e.g., Spear et al., 1999). Because the RSCM thermometer records the maximum temperature achieved by a rock (e.g., Beyssac et al., 2003), the very low temperature at peak pressure inferred by Chatterjee and Jagoutz (2015) is possible because they interpret that temperatures subsequently increased along the exhumation path.

After reaching maximum pressures, the TMN detached and began to be extruded upward via top-down-to-east, normal-sense shearing at its upper boundary (and, presumably, by contemporaneous top-up-to-west, thrust-sense shearing at its lower, unexposed boundary) (Figure 16d). Chatterjee and Jagoutz (2015) interpreted an eclogite facies overprint at ~670–720°C and ~18–19 kbar, but such high temperatures are inconsistent with our RSCM data. Otherwise, a widespread amphibolite facies overprint is interpreted to have occurred at pressures of ~7–10 kbar (~27- to 38-km depths) and temperatures ranging between ~530°C and ~750°C (Chatterjee & Jagoutz, 2015; de Sigoyer et al., 1997; Guillot et al., 1997; St.-Onge et al., 2013; Wilke et al., 2015) (Figures 16a, 16b, and 16d). Our RSCM temperatures are consistent with some estimated temperatures for the amphibolite facies overprint at 580 ± 50°C and 630 ± 50°C (de Sigoyer et al., 1997; Guillot et al., 1997). However, our data and the absence of partial melting rule out some maximum estimated temperatures of ≥700°C (Chatterjee & Jagoutz, 2015; St.-Onge et al., 2013; Wilke et al., 2015; Figure 16a).

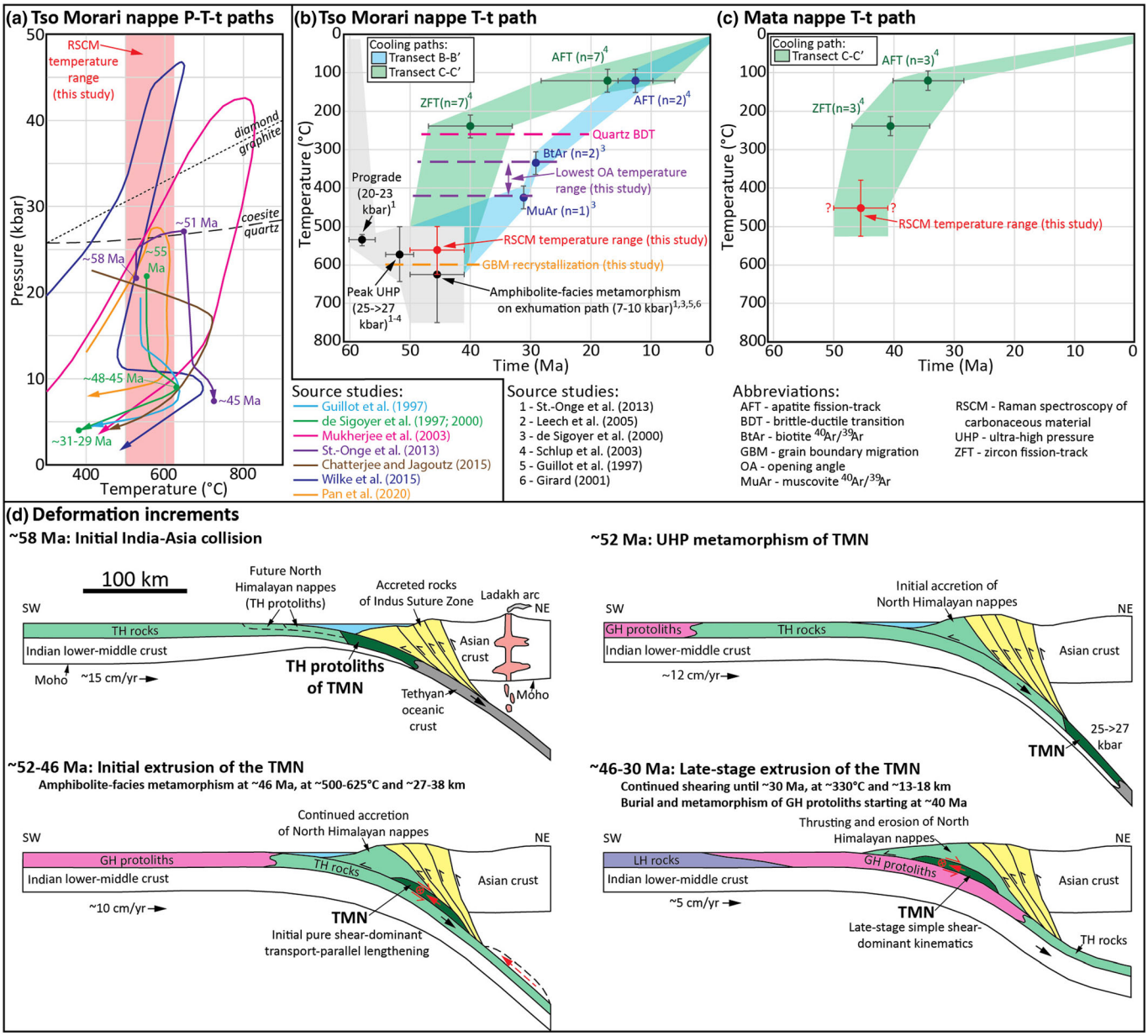

Figure 16. (a) Compilation of published P-T-t paths from the TMN, with our RSCM temperature range from the majority of TMN samples shown for comparison. Most P-T-t data are from samples collected along or proximal to transect C-C′. Available timing constraints are shown for some paths. (b and c) Composite temperature-time paths for the (b) TMN on transects B-B′ and C-C′ and the (c) Mata nappe on transect C-C′, based on published data and new temperature data from our study. The following approximate closure temperature ranges (calculated at orogenic cooling rates of 10–15°C/Myr) were used: 425°C for muscovite $^{40}Ar/^{39}Ar$ (for 100-μm radius muscovite at 10 kbar; Harrison et al., 2009); 335°C for biotite $^{40}Ar/^{39}Ar$ (Grove & Harrison, 1996); 240°C for zircon fission-track (based on field-based investigations of radiation-damaged zircon; Brandon et al., 1998; Bernet, 2009); and 120°C for apatite fission-track (for apatite of average composition; Reiners & Brandon, 2006). A long-term cooling rate of 9.5–15°C/Myr for the TMN, calculated from attainment of 500–625°C peak temperatures at ~50–41 Ma (e.g., de Sigoyer et al., 2000; St.-Onge et al., 2013) to cooling to surface temperatures of 15 ± 10°C at 0 Ma, justifies the use of these closure temperatures. For all four thermochonometric systems, approximate closure temperature error ranges of ±30°C/km were assigned. The brittle-ductile transition for quartz is based on the ~250–270°C lower limit for crystal-plastic deformation (e.g., Dunlap et al., 1997; Stipp et al., 2002; van Daalen et al., 1999). (d) Schematic cross sections illustrating important time increments in the evolution of the India-Asia margin at the longitude of the TMN (the diagrams of the earliest two increments are modified from Epard & Steck, 2008). Timing constraints for metamorphic events and TMN extrusion are discussed in the text. India-Asia convergence rates are from Copley et al. (2010). The cross sections are oriented NE-SW, perpendicular to the orogen; the red circle inscribed with an "x" within the TMN on the bottom two diagrams denotes a component of motion into the page, as the upper shear zone bounding the TMN accommodated top-down-to-east shearing. GH = Greater Himalayan, LH = Lesser Himalayan, TH = Tethyan Himalayan, TMN = Tso Morari nappe, UHP = ultrahigh pressure.

9.3. Duration of Extensional Shearing and Rate of Exhumation

The total duration and rate of extensional exhumation of the TMN depend on the age of maximum UHP conditions, but this age is disputed. Many studies suggest an age of ~51–52 Ma (de Sigoyer et al., 2000; Leech et al., 2005, 2007; St.-Onge et al., 2013), but Donaldson et al. (2013) interpreted an age of ~45 Ma based on a cluster of U-Pb ages for zircon domains that show distinctive trace element patterns. Published Lu-Hf and Sm-Nd ages of garnet from the TMN have large uncertainty (at minimum ±7 Ma; de Sigoyer et al., 2000), while correlation of zircon ages with UHP conditions requires assumptions related to textures (St.-Onge et al., 2013), previous chronologic interpretations (Leech et al., 2005, 2007), or chemistry (Donaldson et al., 2013). For example, in contrast to zircon dating of the Kaghan eclogites in Pakistan (Kaneko et al., 2003), zircons from the TMN with diagnostic inclusions of coesite or other eclogite facies minerals have not been dated. Sparse data indicate an age of 48–46 Ma for amphibolite facies metamorphism (e.g., Epard & Steck, 2008; St.-Onge et al., 2013), implying that extrusion of the TMN and juxtaposition beneath the Tetraogal and Mata nappes at ~27- to 38-km depths was completed by then. Based on these age constraints, proposed exhumation rates for the TMN range from ~1.2 cm/yr (St.-Onge et al., 2013; ~51 Ma maximum pressures) to ~12 cm/yr (Wilke et al., 2015; ~47 Ma maximum pressures).

While our data do not resolve the ongoing debate regarding initial exhumation rates, they do improve our understanding of the range of extensional exhumation temperatures. The highest temperature quartz recrystallization microstructures (grain boundary migration) are consistent with initial top-down-to-east extensional shearing at ~550–650°C (Figure 16b), if we assume the temperature range outlined in Law (2014) for such microstructures is valid for the TMN. This temperature range overlaps with our RSCM temperatures as well as many prior estimates of peak UHP metamorphism and amphibolite facies overprinting (see above). In contrast, however, and excluding potential complications of hydrolytic weakening and local changes in critically resolved shear stress and/or strain rate, our quartz fabric opening angle temperatures ($n = 4$; ~535°C, ~455°C, ~440°C, and ~330°C) indicate that top-down-to-east extensional shearing continued until rocks in the TMN had cooled to ~330°C. This estimate, however, does not take into account the potential effects of pressure on the opening angle thermometer (see Faleiros et al., 2016). If extensional shearing occurred at 5 kbar, the lowest temperature would increase to ~352°C, whereas if shearing took place at 10 kbar the lowest temperature estimate would be ~423°C. Pressures in excess of 10 kbar are unlikely as they would result in calculated deformation temperatures that exceed RSCM temperatures in adjacent specimens. These new estimates, when paired with published cooling ages (de Sigoyer et al., 2000; Schlup et al., 2003), permit us to quantify the longevity of top-down-to-east shearing and associated exhumation-related cooling.

Zircon fission-track ages collected from the TMN along and proximal to transect C-C′ range between 45 ± 2 and 35 ± 2 Ma (Schlup et al., 2003). Zircon fission-track ages indicate the timing of cooling through a closure temperature of ~240°C (calibrated for radiation-damaged zircon at a cooling rate of ~15°C/Myr; Bernet, 2009), which is just below the ~250–270°C crystal-plastic transition for quartz (e.g., Stipp et al., 2002). Therefore, top-down-to-east ductile shearing must have been completed by ~40 ± 5 Ma in the southeastern part of the TMN (Figure 16b), potentially increasing the duration of extrusion-related extensional shearing by as much as 10 Myr. Farther to the northwest, near transect B-B′, muscovite and biotite $^{40}Ar/^{39}Ar$ ages define cooling through closure temperatures of ~425°C (e.g., Harrison et al., 2009, calibrated at a cooling rate of 10°C/Myr) and ~335°C (e.g., Grove & Harrison, 1996) at ~31 and ~29 Ma, respectively (de Sigoyer et al., 2000). Therefore, based on conservative estimates of the low opening angle temperatures obtained from samples collected on transect B-B′, top-down-to-east shearing in the central part of the TMN may have continued until ~30 Ma (Figures 16b and 16d), increasing the duration of extensional shearing by as much as 15 Myr. For both transects, extensional shearing to greenschist facies conditions implies that the TMN was emplaced to shallower levels in the crust than previous estimates of ~27- to 38-km depth at amphibolite facies conditions (e.g., de Sigoyer et al., 2000; Girard, 2001; Guillot et al., 1997; St.-Onge et al., 2013).

9.4. Depth of the Mata Nappe

Our peak temperature data limit the maximum burial depth of the Mata nappe. This depth is important because (as we explain below), when combined with published thermochronometry, it helps constrain the timing of accretion of the TMN at the base of the North Himalayan nappes and provides further support that the top-to-east shearing that exhumed the TMN continued until at least ~30 Ma. On transect B-B′, RSCM

temperatures of ~550°C were obtained at the base of the Mata nappe, and temperatures of ~150°C were obtained at a structural height of ~7 km above the base, defining a field gradient of ~67°C/km (Figure 4). Projecting this field gradient to the paleo-surface defines a minimum paleo-depth of ~2 km for the rocks at the top of the nappe. We note that thermal-mechanical models of UHP metamorphism (Warren et al., 2008a) and extensional settings (Rey et al., 2009) predict very high near-surface thermal gradients during exhumation, up to 65–100°C/km. So, although 67°C/km would represent an unusually warm equilibrium geotherm, it is possible or even likely in the context of transient geotherms formed during extensional shearing. However, even assuming a conservative gradient of 20°C/km and a surface temperature of 10°C still places the top of the Mata nappe at a shallow, maximum depth of ~7 km. Restoration of foliation-normal shortening in the Mata nappe along B-B′ (46% average in the lower 3 km, and 25% average in the upper 3 km; Table 3) increases its structural thickness by 3.5 km. Therefore, accounting for a range of geothermal gradients (67°C/km, yielding a 2-km minimum depth for the top of the nappe, and 20°C/km, yielding a 7-km maximum depth), the measured structural thickness of the Mata nappe (7 km), and restoration of strain (3.5 km) defines a maximum depth range of 12.5–17.5 km for the base of the Mata nappe on B-B′. This depth falls short of the ~27–38 km estimated depth range for amphibolite facies metamorphism in the TMN at ~48–45 Ma (Chatterjee & Jagoutz, 2015; de Sigoyer et al., 2000; Girard, 2001; Guillot et al., 1997; St.-Onge et al., 2013). Thus, an additional ~10–25 km of exhumation of the TMN must have occurred to juxtapose these two nappes after the amphibolite facies overprint at ~45 Ma. This calculation is consistent with quartz fabric opening angle temperatures that indicate continued extensional shearing well below amphibolite facies conditions.

Published apatite fission-track ages also help constrain the duration of extension. Three ages from the basal ~2.5 km of the Mata nappe on transect C-C′ define cooling through ~120°C (e.g., Reiners & Brandon, 2006) between ~40 and ~31 Ma (Schlup et al., 2003) (Figure 16c), requiring that the basal part of the Mata nappe resided at depths of ~6 km or less by that time (assuming a geothermal gradient of 20°C/km). In contrast, at 31–29 Ma (when the base of the Mata nappe was at or below ~120°C), TMN samples ~25 km to the northwest were at temperatures of ~425–335°C (de Sigoyer et al., 2000) (Figure 16b). Because these TMN samples project only ~3 km structurally deeper than the base of the Mata nappe (using present-day thicknesses on Figure 4), this simultaneous ~200–300°C difference in temperature requires that the TMN and the Mata nappe were not juxtaposed until ~30 Ma or later. This provides additional support that the top-to-east extensional shearing that exhumed the TMN continued until at least ~30 Ma (Figure 16d).

9.5. Broader-Scale Kinematics and Strain Partitioning in the Himalaya

The duration of top-to-east, normal-sense ductile shearing that exhumed the TMN has implications for the factors that promoted the exhumation of UHP rocks in the western Himalaya. The TMN was exhumed rapidly from at least ~95- to 103-km to ~27- to 38-km depths between ~54–45 and ~48–45 Ma, defining an exhumation rate of 1.2–12 cm/yr (e.g., de Sigoyer et al., 2000, 2004; Epard & Steck, 2008; Leech et al., 2005, 2007; St.-Onge et al., 2013; Wilke et al., 2015). This exhumation occurred during a period of rapid India-Asia convergence, which was at a rate of ~12–15 cm/yr between ~60–50 Ma and slowed to ~8–9 cm/yr by ~45 Ma (Copley et al., 2010; Molnar & Stock, 2009; van Hinsbergen et al., 2012, 2019). The top-to-east shearing direction recorded in the TMN may be the result of partitioning of strain into components of orogen-subparallel extension and orogen-subnormal shortening, as a consequence of oblique India-Asia convergence proximal to the nascent western syntaxis (e.g., Fossen & Tikoff, 1998; Thompson et al., 1997a, 1997b). This process is similar to the kinematic scenario documented in the western portion of the Himalaya between the middle Miocene and the present, where strain partitioning reflects the westward increase in obliquity between the strike of the orogen and the India-Asia convergence vector (e.g., Fan & Murphy, 2020; McCaffrey & Nabelek, 1998; Murphy & Copeland, 2005; Seeber & Pêcher, 1998; Styron et al., 2011; Whipp et al., 2014).

Following early, rapid exhumation, the TMN continued to be exhumed by top-to-east shearing, from a depth of ~27–38 km (the depth of amphibolite facies metamorphism) to ~12.5–17.5 km (our restored depth of the base of the Mata nappe) between ~48–45 and ~30 Ma (Figure 16d), defining a much slower exhumation rate of 0.6–1.7 mm/yr. This slowdown co-occurred with gradual slowing of India-Asia convergence rates from ~8–9 to ~5–7 cm/yr (Copley et al., 2010; Molnar & Stock, 2009; van Hinsbergen et al., 2012, 2019). Rapid India-Asia convergence has been proposed as a factor that promoted exhumation of UHP rocks during the earliest phases of orogenesis (e.g., Epard & Steck, 2008; Parrish et al., 2006). Whereas rapid convergence may indeed have facilitated rapid exhumation, top-down-to-east ductile shearing and associated

exhumation of the TMN to upper-crustal levels continued for ~15 Myr after the dramatic postcollisional slowing of India-Asia convergence. Thus, long-duration strain partitioning during oblique convergence, during both rapid and slow India-Asia convergence, apparently promoted the exhumation of the TMN and possibly other high-pressure and UHP rocks in the western Himalaya.

9.6. Timing Relationship of UHP Emplacement to Regional Metamorphism

By ~45 Ma, the TMN had been exhumed to amphibolite facies conditions, emplacing it upon structurally lower rocks of the subducting Indian margin. While insufficient structural relief is available in the Tso Morari region to expose these footwall rocks, similarly old eclogites at Kaghan (~46-Ma peak metamorphism; Kaneko et al., 2003; Parrish et al., 2006; Rehman et al., 2016; Spencer & Gebauer, 1996; Tonarini et al., 1993) and Stak (~51-Ma peak metamorphism; Riel et al., 2008) in the western Himalaya in Pakistan were emplaced onto and interfolded with Greater Himalayan rocks (Lanari et al., 2013; LeFort et al., 1997). Elsewhere along the orogen, U-Pb zircon, monazite, and titanite ages from Greater Himalayan rocks increasingly point to high-temperature or peak metamorphism as early as ~40 Ma. Examples include gneiss domes along the southern margin of Tibet (Dala Dome in the eastern portion of the orogen, Aikman et al., 2008; Dai et al., 2020; Ding et al., 2016; Lopu Range in the central portion, Laskowski et al., 2016), structurally high rocks along the crest of the Himalaya (Namche Barwa syntaxis in the eastern portion of the orogen, Zhang et al., 2015; the Marsyandi region in the central portion, Kohn & Corrie, 2011; Walters & Kohn, 2017), as well as Greater Himalayan rocks exposed further to the foreland (Himachal Pradesh, northwestern India; Stübner et al., 2014; Karnali klippe in western Nepal; Braden et al., 2017; Soucy La Roche et al., 2018). Logically, the emplacement of slivers of the earlier subducted Indian margin, such as at Tso Morari, Kaghan, and Stak, locally aided in the structural burial of subducting Greater Himalayan rocks, leading to high-temperature metamorphism by ~40 Ma (Figure 16d).

9.7. Implications for UHP Exhumation

Interpretations of the exhumation of the TMN have focused on the lack of evidence for transformation of the quartzo-feldspathic Puga orthogneiss to eclogite facies mineral assemblages (especially coesite, omphacite, and garnet) and the proximity of low-viscosity serpentinites (de Sigoyer et al., 2004; Epard & Steck, 2008; see, however, Bidgood et al., 2020, for discussion of microstructural evidence of former coesite). The Puga orthogneiss is the dominant exposed lithology in the TMN, and its relatively low bulk density (<3 g/cm^3 for granitic rocks, even with coesite) would have favored detachment from the subducting slab and facilitated upward movement. Proposed mechanisms for exhumation and emplacement include forced corner flow within a low-viscosity subduction interface (de Sigoyer et al., 2004), piston forcing as thicker Indian crust and lithosphere entered and choked the subduction channel (Epard & Steck, 2008), or diapiric rise (Chatterjee & Jagoutz, 2015).

The thermal-mechanical models of Warren et al. (2008a) for continental subduction analogous to the Himalaya are generally consistent with both the P-T-t evolution and the depth of emplacement of the TMN into the crust. For example, subduction to UHP conditions at temperatures of ~600°C and exhumation via upward forcing and extensional shearing to ~10 km require <10 Myr, consistent with (admittedly wide) geochronologic constraints from the TMN. Depending on the physical properties of the crust and mantle and the initial thermal structure, these models show a range of exhumation behaviors, including buoyant rise of UHP rocks during slab roll-back, forced expulsion as thick continental lithosphere enters the subduction zone ("plunger"), or entrainment of UHP rocks into the recirculating wedge above the subducting slab (Warren et al., 2008b). In all cases, UHP rocks move "back" up the subduction zone toward the suture, with substantial cooling in the case of buoyancy-driven uplift, and nearly isothermal exhumation for plunger- and recirculation-driven exhumation. Oceanic subduction models commonly point to the narrowing of the subduction channel and development of a rigid backstop to drive corner flow that exhumes rocks (e.g., Cloos, 1982). Subduction of the leading edge of a continent does not induce corner flow in the models of Warren et al. (2008a, 2008b), but emplacement of UHP rocks closely juxtaposes them with ultramafic rocks, naturally leading to comparisons with oceanic subduction.

Most petrologic data do not favor diapiric rise. As Chatterjee and Jagoutz (2015) discussed, rise of a buoyant sliver of continental crust is expected to drive significant heating of the diapir. In their interpretations, a rise in temperature of ~300°C at high but decreasing pressure represents the transfer of the TMN from the

relatively cold subduction interface to the hotter region of the convecting mantle. However, there is little evidence to support such a large temperature increase. Most data indicate maximum pressures at temperatures of ~600°C (e.g., de Sigoyer et al., 1997; Guillot et al., 1997; Pan et al., 2020; Sachan et al., 2004; St.-Onge et al., 2013), which are comparable to our RSCM temperatures (Figure 16a). Because RSCM thermometry records the maximum temperature that a rock attains, there is little latitude for a temperature increase that might represent vertical diapiric rise. Rather, isothermal exhumation would seem to better approximate the overall P-T path, and this is more consistent with other mechanisms, especially the recirculation and plunger models of Warren et al. (2008a, 2008b).

Available petrochronologic data from the TMN are too uncertain either analytically or interpretationally to favor one exhumation mechanism over another. For example, modeling of diffusive relaxation of calcium gradients in garnet has been used to suggest a duration of 0.03–0.09 Myr at a temperature of 720°C (Chatterjee & Jagoutz, 2015). However, for typical activation energies for divalent cation diffusion in garnet (e.g., Carlson, 2006; Chu & Ague, 2015), a lower peak temperature of 600°C increases the possible duration by a factor of 50–150 or ~2–10 Myr (assuming 0.06 ± 0.03 times 100 ± 50, and propagating errors). Other estimates of the timing of peak UHP conditions in the TMN either differ substantially for zircon U-Pb ages (53.3 ± 0.7 Ma, Leech et al., 2005; 50.8 ± 1.4 Ma, St.-Onge et al., 2013; ~43–47 Ma, Donaldson et al., 2013) or are highly uncertain for garnet ages (55 ± 12 and 55 ± 7 Ma, de Sigoyer et al., 2000). Ages of amphibolite facies metamorphism also are either highly interpretational (see discussion in Donaldson et al., 2013; 47.0 ± 0.5 Ma, Guillot et al., 2008; 45.3 ± 1.1, St.-Onge et al., 2013) or bear large uncertainties (47 ± 6 Ma, de Sigoyer et al., 2004). Thus, the duration of exhumation from peak UHP to amphibolite facies conditions could range from ~0 to ~10 Myr. This uncertainty leads to large variations in possible exhumation rates (~1 cm/yr to near-instantaneous) that may or may not be compatible with models of UHP exhumation processes (~1–2 cm/yr; Warren et al., 2008b).

10. Conclusions

1. The 5.5-km-thick TMN represents the exposed upper portion of a ductile slab that was extruded via distributed, top-down-to-east, normal-sense ductile shearing, as indicated by shear-sense indicators, high-strength quartz CPOs (cylindricity values of 0.65–0.97; density norm values of 1.74–2.86) and finite strain data that define 63% average transport-parallel lengthening and 46% average transport-normal shortening. The TMN experienced an accelerating strain path, with pure shear-dominant flattening strain (W_m = 0.00–0.45) that progressed to late-stage, simple shear-dominant plane-strain shearing (W_n = 0.90–0.99).
2. The TMN attained peak temperatures of ~500–625°C, and temperatures in overlying nappes decrease upward to as low as ~150°C, defining an upright field gradient locally as steep as 67°C/km. An upright strain gradient is observed across the top 1 km of the TMN and basal 2 km of overlying nappes, with cylindricity values decreasing to 0.25–0.31, density norm values decreasing to 1.14–1.21, and transport-parallel lengthening and transport-normal shortening decreasing upward to 14% and 18%, respectively.
3. Quartz CPO deformation temperatures along the exhumation path are as low as ~330 ± 50°C, indicating that top-to-east shearing continued until the TMN cooled through ~425–335°C at ~30 Ma. Protracted extensional exhumation is also supported by our reconstructed 12.5- to 17.5-km maximum depth of the base of the Mata nappe, which, when combined with published thermochronometry, requires that the TMN was not underplated at upper-crustal levels until ~30 Ma. Long-duration, convergence-subnormal, extensional shearing outlasted rapid India-Asia convergence by ~15 Myr and may be attributed to strain partitioning during oblique convergence, similar to the Miocene-present kinematic scenario of the western Himalaya.
4. Subduction metamorphism of the TMN to UHP conditions and exhumation to middle or upper crustal levels are generally consistent with models that emphasize piston forcing ("plunger") or recirculation, but less consistent with buoyancy-dominated exhumation, corner flow, or diapiric rise. Available geochronologic constraints on peak UHP metamorphism in the TMN are too broad to constrain rates of exhumation that might distinguish among models.
5. Emplacement of the TMN on (likely) Greater Himalayan rocks of the Indian continental margin plausibly drove prograde metamorphism until 40 Ma, as suggested by petrochronologic data in the eastern

and central portions of the orogen. Further work on the timing of prograde metamorphism of the Mata nappe and the Greater Himalayan Sequence in the western Himalaya would help elucidate the timing relationship between exhumation of the TMN and propagating prograde metamorphism toward the foreland.

Data Availability Statement

All of the data used for this research are contained within the manuscript and supplementary material. The data used for this research have been placed in the online data repository Zenodo (https://zenodo.org/record/4287542#.X7wSvrN7mUk) (https://doi.org/10.5281/zenodo.4287542).

Acknowledgments

This work was supported by start-up funds awarded to S. Long from the Washington State University School of the Environment, as well as grants EAR1450507 and OIA1545903 awarded to MJK from the US National Science Foundation. We sincerely thank Dr. Talat Ahmad, Dr. Reyaz Ahmad Dar, Irfan Bhat, and Gulam Nabiley for assistance with travel logistics, permitting, field work, and sample shipping. We would like to thank associate editor Djordje Grujic and reviewers Richard Palin and Paris Xypolias for constructive and thoughtful reviews.

References

Aikman, A. B., Harrison, T. M., & Ding, L. (2008). Evidence for Early (>44 Ma) Himalayan crustal thickening, Tethyan Himalaya, southeastern Tibet. *Earth and Planetary Science Letters*, *274*(1–2), 14–23. https://doi.org/10.1016/j.epsl.2008.06.038

Bailey, J. E., & Hirsch, P. B. (1962). The recrystallization process in some polycrystalline metals. *Proclamations of the Royal Society of London*, *A267*, 11–30.

Barth, N., Hacker, B., Seward, G., Walsh, E., Young, D., & Johnston, S. (2010). Strain within the ultrahigh pressure Western Gneiss Region of Norway recorded by quartz CPOs. In R. D. Law, R. W. H. Butler, R. Holdsworth, M. Krabbendam, R. A. Strachan (Eds.), *Continental tectonics and mountain building—The legacy of Peach and Horne*, *Special Publication* (Vol. 335, pp. 663–685). London: Geological Society. https://doi.org/10.1144/SP335.24

Beaumont, C., Jamieson, R. A., Butler, J. P., & Warren, C. J. (2009). Crustal structure: A key constraint on the mechanism of ultra-high-pressure rock exhumation. *Earth and Planetary Science Letters*, *287*(1–2), 116–129. https://doi.org/10.1016/j.epsl.2009.08.001

Bernet, M. (2009). A field-based estimate of the zircon fission-track closure temperature. *Chemical Geology*, *259*(3–4), 181–189. https://doi.org/10.1016/j.chemgeo.2008.10.043

Berthelsen, A. (1953). On the geology of the Rupshu district, N.W. Himalaya. *Meddelelser fra Dansk Geologisk Forening (København)*, *12*, 351–414.

Beyssac, O., Goffe, B., Chopin, C., & Rouzaud, J. (2002). Raman spectra of carbonaceous material in metasediments: A new geothermometer. *Journal of Metamorphic Geology*, *20*(9), 859–871. https://doi.org/10.1046/j.1525-1314.2002.00408.x

Beyssac, O., Goffe, B., Petitet, J. P., Froigneux, E., Moreau, M., & Rouzaud, J. N. (2003). On the characterization of disordered and heterogeneous carbonaceous materials by Raman spectroscopy. *Spectrochimica Acta Part A*, *59*(10), 2267–2276. https://doi.org/10.1016/S1386-1425(03)00070-2

Bidgood, A. K., Parsons, A. J., Lloyd, G. E., Waters, D. J., & Goddard, R. M. (2020). EBSD-based criteria for coesite-quartz transformation. *Journal of Metamorphic Geology*, 16. https://doi.org/10.1111/jmg.12566

Bouchez, J. L., Lister, G. S., & Nicolas, A. (1983). Fabric asymmetry and shear sense in movement zones. *Geologische Rundschau*, *72*(2), 401–419. https://doi.org/10.1007/BF01822075

Braden, Z., Godin, L., & Cottle, J. M. (2017). Segmentation and rejuvenation of the Greater Himalayan sequence in western Nepal revealed by in situ U-Th/Pb monazite petrochronology. *Lithos*, *284–285*, 751–765.

Brandon, M. T., Roden-Tice, M. K., & Garver, J. I. (1998). Late Cenozoic exhumation of the Casdacia accretionary wedge in the Olympic Mountains, northwest Washington State. *Geological Society of America Bulletin*, *110*(8), 985–1009. https://doi.org/10.1130/0016-7606(1998)110<0985:LCEOTC>2.3.CO;2

Buchs, N., & Epard, J.-L. (2019). Geology of the eastern part of the Tso Morari nappe, the Nidar Ophiolite and the surrounding tectonic units (NW Himalaya, India). *Journal of Maps*, *15*(2), 38–48. https://doi.org/10.1080/17445647.2018.1541196

Carlson, W. D. (2006). Rates of Fe, Mg, Mn, and Ca diffusion in garnet. *American Mineralogist*, *91*(1), 1–11. https://doi.org/10.2138/am.2006.2043

Chatterjee, N., & Jagoutz, O. (2015). Exhumation of the UHP Tso Morari eclogite as a diapir rising through the mantle wedge. *Contributions to Mineralogy and Petrology*, *169*(1), 3. https://doi.org/10.1007/s00410-014-1099-y

Chemenda, A. I., Mattauer, M., Malavieille, J., & Bokun, A. N. (1995). A mechanism for syn-collisional rock exhumation and associated normal faulting: Results from physical modelling. *Earth and Planetary Science Letters*, *132*(1–4), 225–232. https://doi.org/10.1016/0012-821X(95)00042-B

Chopin, C. (2003). Ultrahigh-pressure metamorphism: Tracing continental crust into the mantle. *Earth and Planetary Science Letters*, *212*(1–2), 1–14. https://doi.org/10.1016/S0012-821X(03)00261-9

Chu, X., & Ague, J. J. (2015). Analysis of experimental data on divalent cation diffusion kinetics in aluminosilicate garnets with application to timescales of peak Barrovian metamorphism, Scotland. *Contributions to Mineralogy and Petrology*, *170*(2), 25. https://doi.org/10.1007/s00410-015-1175-y

Cloos, M. (1982). Flow melanges: Numerical modeling and geologic constraints on their origin in the Franciscan subduction complex, California. *Geological Society of America Bulletin*, *93*(4), 330–344. https://doi.org/10.1130/0016-7606(1982)93<330:FMNMAG>2.0.CO;2

Copley, A., Avouac, J.-P., & Royer, J.-Y. (2010). India-Asia collision and the Cenozoic slowdown of the Indian plate: Implications for the forces driving plate motions. *Journal of Geophysical Research*, *115*, B03410. https://doi.org/10.1029/2009JB006634

Dai, Z., Dong, L., Li, G., Huizenga, J. M., Ding, J., Zhang, L., et al. (2020). Crustal thickening prior to 43 Ma in the Himalaya: Evidence from lower crust-derived adakitic magmatism in Dala, eastern Tethyan Himalaya, Tibet. *Geological Journal*, *55*(5), 4021–4046. https://doi.org/10.1002/gj.3639

de Sigoyer, J. (1998). Mécanismes d'exhumation des roches de haute pression basse température, en contexte de convergence continentale (Tso Morari, NO Himalaya): [Ph.D. dissertation] Université Claude Bernard, Lyon, France, p. 236.

de Sigoyer, J., Chavagnac, V., Blichert-Toft, J., Villa, I. M., Luais, P., Guillot, S., et al. (2000). Dating the Indian continental subduction and collisional thickening in the northwest Himalaya: Multichronology of the Tso Morari eclogites. *Geology*, *28*(6), 487–490. https://doi.org/10.1130/0091-7613(2000)28<487:DTICSA>2.0.CO;2

de Sigoyer, J., Guillot, S., & Dick, P. (2004). Exhumation of the ultrahigh-pressure Tso Morari unit in eastern Ladakh (NW Himalaya): A case study. *Tectonics*, *23*, TC3003. https://doi.org/10.1029/2002TC001492

de Sigoyer, J., Guillot, S., Lardeaux, J. M., & Mascle, G. (1997). Glaucophane-bearing eclogites in the Tso Morari dome (eastern Ladakh, NW Himalaya). *European Journal of Mineralogy*, *9*(5), 1073–1084. https://doi.org/10.1127/ejm/9/5/1073

Ding, H., Zhang, Z., Dong, X., Tian, Z., Xiang, H., Mu, H., et al. (2016). Early Eocene (c. 50 Ma) collision of the Indian and Asian continents: Constraints from the north Himalayan metamorphic rocks, southeastern Tibet. *Earth and Planetary Science Letters*, *435*, 64–73. https://doi.org/10.1016/j.epsl.2015.12.006

Donaldson, D. G., Webb, A. A. G., Menold, C. A., Kylander-Clark, A. R. C., & Hacker, B. R. (2013). Petrochronology of Himalayan ultrahigh-pressure eclogite. *Geology*, *41*(8), 835–838. https://doi.org/10.1130/G33699.1

Draganits, E., Grasemann, B., Frank, W., Miller, C., & Wiesmayr, G. (1998). The sedimentary protoliths of the HHC in the Chamba–Lahaul area, NW Himalayas, India: *HKT-workshop Abstracts. Geological Bulletin University of Peshawar*, *31*, 58–60.

Drury, M. R., Humphreys, F. J., & White, S. H. (1985). Large strain deformation studies using polycrystalline magnesium as rock analogue, part II: Dynamic recrystallization mechanisms at high temperatures. *Physics of the Earth and Planetary Interiors*, *40*(3), 208–222. https://doi.org/10.1016/0031-9201(85)90131-1

Dunlap, W. J., Hirth, G., & Teyssier, C. (1997). Thermomechanical evolution of a ductile duplex. *Tectonics*, *16*(6), 983–1000. https://doi.org/10.1029/97TC00614

Dunnet, D. (1969). A technique for finite strain analysis using elliptical particles. *Tectonophysics*, *7*(2), 117–136. https://doi.org/10.1016/0040-1951(69)90002-X

Dutta, D., & Mukherjee, S. (2020). Extrusion kinematics of UHP terrain in collisional orogen: EBSD and microstructure-based approach from Tso Morari Crystallines, Ladakh Himalaya. *Tectonophysics*. https://doi.org/10.1016/j.tecto.2020.228641

Epard, J.-L., & Steck, A. (2004). The eastern prolongation of the Zanskar shear zone (Western Himalaya). *Eclogae Geologicae Helvetiae*, *97*(2), 193–212. https://doi.org/10.1007/s00015-004-1116-7

Epard, J.-L., & Steck, A. (2008). Structural development of the Tso Morari ultra-high pressure nappe of the Ladakh Himalaya. *Tectonophysics*, *451*(1–4), 242–264. https://doi.org/10.1016/j.tecto.2007.11.050

Faleiros, F. M., Moraes, R., Pavan, M., & Campanha, G. A. C. (2016). A new empirical calibration of the quartz *c*-axis fabric opening-angle deformation thermometer. *Tectonophysics*, *671*, 173–182. https://doi.org/10.1016/j.tecto.2016.01.014

Fan, S., & Murphy, M. A. (2020). Three-dimensional strain accumulation and partitioning in an arcuate orogenic wedge: An example from the Himalaya. *Geological Society of America Bulletin*. https://doi.org/10.1130/B35528.1

Fossen, H., & Tikoff, B. (1993). The deformation matrix for simultaneous simple shearing, pure shearing and volume change, and its application to transpression–transtension tectonics. *Journal of Structural Geology*, *15*(3–5), 413–422. https://doi.org/10.1016/0191-8141(93)90137-Y

Fossen, H., & Tikoff, B. (1998). Extended models of transpression and transtension, and applications to tectonic settings. In R. E. Holdsworth, R. A. Strachan, J. R. Dewey (Eds.), *Continental transpressional and transtensional tectonics*, *Special Publication* (Vol. 135, pp. 15–33). London: Geological Society.

Fuchs, G., & Linner, M. (1996). On the geology of the suture zone and Tso Morari dome in eastern Ladakh (Himalaya). *Jahrbuch der Geologischen Bundesanstalt, Wien*, *139*, 191–207.

Gansser, A. (1964). *Geology of the Himalayas* (p. 289). New York: Wiley-Interscience.

Girard, M. (2001). *Metamorphism and tectonics of the transition between nonmetamorphic Tethyan Himalaya sediments and the north Himalayan crystalline zone (Rupshu area, Ladakh, NW India)*, *Memoires de Géologie (Lausane)* (Vol. 35, pp. 1–100). Switzerland: Lausanne.

Girard, M., & Bussy, F. (1999). Late Pan-African magmatism in the Himalaya: New geochronological and geochemical data from the Ordovician Tso Morari metagranites (Ladakh, NW India). *Schweizerische Mineralogische und Petrographische Mitteilungen*, *79*, 399–417.

Gouzu, C., Itaya, T., Hyodo, H., & Ahmad, T. (2006). Cretaceous isochron ages from K-Ar and $^{40}Ar/^{39}Ar$ dating of eclogitic rocks in the Tso Morari complex, western Himalaya, India. *Gondwana Research*, *9*(4), 426–440. https://doi.org/10.1016/j.gr.2006.01.002

Grove, M., & Harrison, T. M. (1996). $^{40}Ar^*$ diffusion in Fe-rich biotite. *American Mineralogist*, *81*(7–8), 940–951. https://doi.org/10.2138/am-1996-7-816

Guillope, M., & Poirier, J. P. (1979). Dynamic recrystallization during creep of single-crystalline halite: An experimental study. *Journal of Geophysical Research*, *84*(B10), 5557–5567. https://doi.org/10.1029/JB084iB10p05557

Guillot, S., De Sigoyer, J., Lardeaux, J. M., & Mascle, G. (1997). Eclogitic metasediments from the Tso Morari area (Ladakh Himalaya): Evidence for continental subduction during India–Asia convergence. *Contributions to Mineralogy and Petrology*, *128*(2–3), 197–212. https://doi.org/10.1007/s004100050303

Guillot, S., Maheo, G., de Sigoyer, J., Hattori, K. H., & Pecher, A. (2008). Tethyan and Indian subduction viewed from the Himalayan high- to ultrahigh-pressure metamorphic rocks. *Tectonophysics*, *451*, 225–241.

Hacker, B. R., Gerya, T. V., & Gilotti, J. A. (2013). Formation and exhumation of ultrahigh-pressure terranes. *Elements*, *9*(4), 289–293. https://doi.org/10.2113/gselements.9.4.289

Harrison, T. M., Celerier, J., Aikman, A. B., Hermann, J., & Heizler, M. T. (2009). Diffusion of ^{40}Ar in muscovite. *Geochimica et Cosmochimica Acta*, *73*(4), 1039–1051. https://doi.org/10.1016/j.gca.2008.09.03

Honegger, K., Dietrich, V., Frank, W., Gansser, A., Thöni, M., & Trommsdorff, V. (1982). Magmatism and metamorphism in the Ladakh Himalayas (the Indus-Tsangpo suture zone). *Earth and Planetary Science Letters*, *60*(2), 253–292. https://doi.org/10.1016/0012-821X(82)90007-3

Horton, F., Lee, J., Hacker, B., Bowman-Kamaha'o, M., & Cosca, M. (2015). Himalayan gneiss dome formation in the middle crust and exhumation by normal faulting: New geochronology of Gianbul dome, northwestern India. *Geological Society of America Bulletin*, *127*(1–2), 162–180. https://doi.org/10.1130/B31005.1

Hunter, N. J. R., Hasalova, P., Weinberg, R., Wilson, C. J. L., & Luzin, V. (2015). Using the 'crystal signature' of mylonites to demarcate the Main central thrust (Alaknanda region, Garhwal Himalaya). *Himalayan-Karakorum-Tibet Workshop Abstract, Dehradun, India*, 69–71.

Hunter, N. J. R., Weinberg, R. F., Wilson, C. J. L., Luzin, V., & Misra, S. (2018). Microscopic anatomy of a 'hot-on-cold' shear zone: Insights from quartzites of the main central thrust in the Alaknanda region (Garhwal Himalaya). *Geological Society of America Bulletin*, *130*(9–10), 1519–1539. https://doi.org/10.1130/B31797.1

Johnson, S. E., Lenferink, H. J., Price, N. A., Marsh, J. H., Koons, P. O., West, D. P. Jr., & Beane, R. (2009). Clast-based kinematic vorticity gauges: The effects of slip at matrix/clast interfaces. *Journal of Structural Geology*, *31*(11), 1322–1339. https://doi.org/10.1016/j.jsg.2009.07.008

Kaneko, Y., Katayama, I., Yamamoto, H., Misawa, K., Ishikawa, M., Rehman, H. U., et al. (2003). Timing of Himalayan ultrahigh-pressure metamorphism: Sinking rate and subduction angle of the Indian continental crust beneath Asia. *Journal of Metamorphic Geology*, *21*(6), 589–599. https://doi.org/10.1046/j.1525-1314.2003.00466.x

Kilian, R., & Heilbronner, R. (2017). Analysis of crystallographic preferred orientations of experimentally deformed Black Hills quartzite. *Solid Earth*, *8*(5), 1095–1117. https://doi.org/10.5194/se-8-1095-2017

Kohn, M. J., & Corrie, S. L. (2011). Preserved Zr-temperatures and U-Pb ages in high-grade metamorphic titanite: Evidence for a static hot channel in the Himalayan orogen. *Earth and Planetary Science Letters*, *311*(1–2), 136–143. https://doi.org/10.1016/j.epsl.2011.09.008

Kruhl, J. H. (1998). Prism- and basal-plane parallel subgrain boundaries in quartz: A microstructural geothermobarometer: Reply. *Journal of Metamorphic Geology*, *16*, 142–146.

Kylander-Clark, A. R. C., Hacker, B. R., & Mattinson, C. G. (2012). Size and exhumation rate of ultrahigh-pressure terranes linked to orogenic stage. *Earth and Planetary Science Letters*, *321-322*, 115–120. https://doi.org/10.1016/j.epsl.2011.12.036

Lanari, P., Riel, N., Guillot, S., Vidal, O., Schwartz, S., Pecher, A., & Hattori, K. H. (2013). Deciphering high-pressure metamorphism in collisional context using microprobe mapping methods: Application to the Stak eclogitic massif (northwest Himalaya). *Geology*, *41*(2), 111–114. https://doi.org/10.1130/G33523.1

Larson, K. P. (2018). Refining the structural framework of the Khimti Khola region, east-Central Nepal Himalaya, using quartz textures and *c*-axis fabrics. *Journal of Structural Geology*, *107*, 142–152. https://doi.org/10.1016/j.jsg.2017.12.014

Larson, K. P. (2020). Quartz c-axis processing scripts in R. https://doi.org/10.17605/OSF.IO/MJTXV

Larson, K. P., Cottle, J., Lederer, G., & Rai, S. M. (2017). Defining shear zone boundaries using fabric intensity gradients: An example from the east-Central Nepal Himalaya. *Geosphere*, *13*(3), 771–781. https://doi.org/10.1130/GES01373.1

Larson, K. P., & Godin, L. (2009). Kinematics of the greater Himalayan sequence, Dhaulagiri Himal: Implications for the structural framework of Central Nepal. *Journal of the Geological Society of London*, *166*(1), 25–43. https://doi.org/10.1144/0016-76492007-180

Laskowski, A. K., Kapp, P., & Ding, L. (2016). High-pressure Tethyan Himalaya rocks along the India-Asia suture zone in southern Tibet. *Lithosphere*, *8*(5), 574–582. https://doi.org/10.1130/L544.1

Law, R. D. (2010). Moine thrust zone mylonites at the stack of Glencoul: II - results of vorticity analyses and their tectonic significance. In R. D. Law, R. W. H. Butler, R. Holdsworth, M. Krabbendam, R. A. Strachan (Eds.), *Continental Tectonics and Mountain Building - the Legacy of Peach and Horne*, *Special Publication* (Vol. 335, pp. 579–602). London: Geological Society. https://doi.org/10.1144/SP335.24

Law, R. D. (2014). Deformation thermometry based on quartz *c*-axis fabrics and recrystallization microstructures: A review. *Journal of Structural Geology*, *66*, 129–161. https://doi.org/10.1016/j.jsg.2014.05.023

Law, R. D., Searle, M. P., & Simpson, R. L. (2004). Strain, deformation temperatures and vorticity of flow at the top of the greater Himalayan slab, Everest massif, Tibet. *Journal of the Geological Society of London*, *161*(2), 305–320. https://doi.org/10.1144/0016-764903-047

Law, R. D., Stahr, D. W., Francsis, M. K., Ashley, K. T., Grasemann, B., & Ahmad, T. (2013). Deformation temperatures and flow vorticities near the base of the Greater Himalayan Series, Sutlej Valley and Shimla Klippe, NW India. *Journal of Structural Geology*, *54*, 21–53. https://doi.org/10.1016/j.jsg.2013.05.009

Leech, M. L., Sing, S., Jain, A. K., Klemperer, R. M., & Manickavasagam, R. M. (2005). The onset of India–Asia continental collision: Early, steep subduction required by the timing of UHP metamorphism in the western Himalaya. *Earth and Planetary Science Letters*, *234*(1–2), 83–97. https://doi.org/10.1016/j.epsl.2005.02.038

Leech, M. L., Singh, S., & Jain, A. K. (2007). Continuous metamorphic zircon growth and interpretation of U-Pb SHRIMP dating: An example from the western Himalaya. *International Geology Review*, *49*, 313–328.

LeFort, P. (1975). Himalayas: The collided range, present knowledge of the continental arc. *American Journal of Science*, *275-A*, 1–44.

LeFort, P., Guillot, S., & Pecher, A. (1997). HP metamorphic belt along the Indus suture zone of NW Himalaya: New discoveries and significance. *Comptes Rendus de l'Academie des Sciences, Paris*, *325*, 773–778.

Lister, G. S., & Hobbs, B. E. (1980). The simulation of fabric development during plastic deformation and its application to quartzite: The influence of deformation history. *Journal of Structural Geology*, *2*(3), 355–370. https://doi.org/10.1016/0191-8141(80)90023-1

Lister, G. S., & Williams, P. F. (1979). Fabric development in shear zones: Theoretical controls and observed phenomena. *Journal of Structural Geology*, *1*(4), 283–297. https://doi.org/10.1016/0191-8141(79)90003-8

Long, S., McQuarrie, N., Tobgay, T., & Hawthorne, J. (2011). Quantifying internal strain and deformation temperature in the eastern Himalaya, Bhutan: Implications for the evolution of strain in thrust sheets. *Journal of Structural Geology*, *33*(4), 579–608. https://doi.org/10.1016/j.jsg.2010.12.011

Long, S. P., Gordon, S. M., & Soignard, E. (2017). Distributed north-vergent shear and flattening through greater and Tethyan Himalayan rocks: Insights from metamorphic and strain data from the Dang Chu Region, Central Bhutan. *Lithosphere*, *9*(5), 774–795. https://doi.org/10.1130/L655.1

Long, S. P., Mullady, C. L., Starnes, J. K., Gordon, S. M., Larson, K. P., Miller, R. B., et al. (2019). A structural model for the south Tibetan detachment system in northwestern Bhutan from integration of temperature, fabric, strain, and kinematic data. *Lithosphere*, *11*(4), 465–487. https://doi.org/10.1130/L1049.1

Mainprice, D., Bachman, F., Hielscher, R., & Schaeben, H. (2015). *Descriptive tools for the analysis of texture projects with large datasets using MTEX: Strength, symmetry and components*, *Special Publication* (Vol. 409, pp. 251–271). London: Geological Society. https://doi.org/10.1144/SP409/8

Marti, S., Stünitz, H., Heilbronner, R., Plümper, O., & Kilian, R. (2018). Syn-kinematic hydration reactions, dissolution-precipitation creep and grain boundary sliding in experimentally deformed plagioclase-pyroxene mixtures. *Solid Earth Discussions*, *9*(4), 985–1009. https://doi.org/10.5194/se-2018-39

McCaffrey, R., & Nabelek, J. (1998). Role of oblique convergence in the active deformation of the Himalayas and southern Tibet Plateau. *Geology*, *26*(8), 691–694. https://doi.org/10.1130/0091-7613(1998)026<0691:ROOCIT>2.3.CO;2

Means, W. D. (1994). Rotational quantities in homogeneous flow and the development of small-scale structures. *Journal of Structural Geology*, *17*, 893–896.

Means, W. D., Hobbs, B. E., Lister, G. S., & Williams, P. F. (1980). Vorticity and noncoaxiality in progressive deformation. *Journal of Structural Geology*, *2*(3), 371–378. https://doi.org/10.1016/0191-8141(80)90024-3

Molnar, P., & Stock, J. M. (2009). Slowing of India's convergence with Eurasia since 20 ma and its implications for Tibetan mantle dynamics. *Tectonics*, *28*, TC3001. https://doi.org/10.1029/2008TC002271

Morgan, S., & Law, R. D. (2004). Unusual transition in quartzite dislocation creep regimes and crystal slip systems in the aureole of the Eureka Valley-Joshua flat-Beer Creek pluton, California: A case for anhydrous conditions created by decarbonation reactions. *Tectonophysics*, *384*(1–4), 209–231. https://doi.org/10.1016/j.tecto.2004.03.016

Mukherjee, B., Sachan, H. K., Ogasawaray, Y., Muko, A., & Yoshioka, N. (2003). Carbonate-bearing UHPM rocks from the Tso-Morari region, Ladakh, India: Petrological implications. *International Geology Review*, *45*(1), 49–69. https://doi.org/10.2747/0020-6814.45.1.49

Mukherjee, B. K., & Sachan, J. K. (2001). Discovery of coesite from Indian Himalaya: A record of ultra-high pressure metamorphism in Indian continental crust. *Current Science*, *81*, 1358–1361.

Murphy, M. A., & Copeland, P. (2005). Transtensional deformation in the central Himalaya and its role in accommodating growth of the Himalayan orogen. *Tectonics*, *24*, TC4012. https://doi.org/10.1029/2004TC001659

Nanda, M. M., & Singh, M. P. (1977). Stratigraphy and sedimentation of the Zanskar area, Ladakh and adjoining parts of the Lahul region of Himachal Pradesh. *Himalayan Geology (Dehra Dun)*, *6*, 365–388.

O'Brien, P. J. (2018). Eclogites and other high-pressure rocks in the Himalaya: Location, formation, preservation and tectonometamorphic interpretation. In P. J. Treloar, & M. P. Searle (Eds.), *Himalayan Tectonics: A Modern Interpretation*, *Special Publication* (Vol. 483, pp. 183–213). London: Geological Society. https://doi.org/10.1144/SP483.13

Palin, R. M., St.-Onge, M. R., Waters, D. J., Searle, M. P., & Dyck, B. (2014). Phase equilibria modelling of retrograde amphibole and clinozoisite in mafic eclogite from the Tso Morari massif, Northwest India: Constraining the P–T–M(H_2O) conditions of exhumation. *Journal of Metamorphic Geology*, *32*(7), 675–693. https://doi.org/10.1111/jmg.12085

Pan, R., Macris, C. A., & Menold, C. A. (2020). Thermodynamic modeling of high-grade metabasites: A case study using the Tso Morari UHP eclogite. *Contributions to Mineralogy and Petrology*, *175*(8), 28–78. https://doi.org/10.1007/s00410-020-01717-w

Parrish, R. R., Gough, S. J., Searle, M. P., & Waters, D. J. (2006). Plate velocity exhumation of ultrahigh-pressure eclogites in the Pakistan Himalaya. *Geology*, *34*(11), 989–992. https://doi.org/10.1130/G22796A.1

Passchier, C. W. (1987). Stable positions of rigid objects in non-coaxial flow—A study in vorticity analysis. *Journal of Structural Geology*, *124*, 211–222.

Passchier, C. W., & Trouw, R. A. J. (2005). *Micro-Tectonics* (2nd ed. p. 366). New York: Springer.

Poirier, J. P., & Nicolas, A. (1975). Deformation-induced recrystallization by progressive misorientation of subgrain-boundaries, with special reference to mantle peridotites. *Journal of Geology*, *83*(6), 707–720. https://doi.org/10.1086/628163

Price, R. A. (1972). The distinction between displacement and distortion in flow, and the origin of diachronism in tectonic overprinting in orogenic belts. In J. E. Gill (Ed.), *International Geological Congress Section 3* (Vol. 24, pp. 545–551). Montreal: Union of Geological Sciences.

Rahl, J. M., Anderson, K. M., Brandon, M. T., & Fassoulas, C. (2005). Raman spectroscopic carbonaceous material thermometry of low-grade metamorphic rocks: Calibration and application to tectonic exhumation in Crete, Greece. *Earth and Planetary Science Letters*, *240*(2), 339–354. https://doi.org/10.1016/j.epsl.2005.09.055

Ramsay, J. G. (1967). *Folding and fracturing of rocks* (p. 560). New York: McGraw-Hill.

Ramsay, J. G., & Huber, M. I. (1983). *Techniques of modern structural geology, Vol. 1: Strain Analysis* (p. 307). London: Academic Press.

Rehman, H. U., Lee, H. Y., Chung, S. L., Khan, T., O'Brien, P. J., & Yamamoto, H. (2016). Source and mode of the Permian Panjal trap magmatism: Evidence from zircon U-Pb and Hf isotopes and trace element data from the Himalayan ultrahigh-pressure rocks. *Lithos*, *260*, 286–299. https://doi.org/10.1016/j.lithos.2016.06.001

Rehman, H. U., Yamamoto, H., Khalil, M. A. K., Nakamura, E., Zafar, M., & Khan, T. (2008). Metamorphic history and tectonic evolution of the Himalayan UHP eclogites in Kaghan Valley, Pakistan. *Journal of Mineralogical and Petrological Sciences*, *103*, 242–254.

Reiners, P. W., & Brandon, M. T. (2006). Using thermochronology to understand orogenic erosion. *Annual Review of Earth and Planetary Sciences*, *34*(1), 419–466. https://doi.org/10.1146/annurev.earth.34.031405.125202

Rey, P. F., Teyssier, C., & Whitney, D. L. (2009). Extension rates, crustal melting, and core complex dynamics. *Geology*, *37*(5), 391–394. https://doi.org/10.1130/G25460A.1

Riel, N., Hattori, K., Guillot, S., Rayner, N., Davis, B., Latif, M., & Kausar, A. B. (2008). SHRIMP zircon ages of eclogites in the Stak massif, northern Pakistan. *Himalayan Journal of Sciences*, *5*(7), 119–120.

Sachan, H. K., Mukherjee, B. K., Ogasawara, Y., Maruyama, S., Ishida, H., Muko, A., & Yoshioka, N. (2004). Discovery of coesite from Indus suture zone (ISZ), Ladakh, India: Evidence for deep subduction. *European Journal of Mineralogy*, *16*(2), 235–240. https://doi.org/10.1127/0935-1221/2004/0016-0235

Schlup, M., Carter, A., Cosca, M., & Steck, A. (2003). Exhumation history of eastern Ladakh revealed by $^{40}Ar/^{39}Ar$ and fission track ages: The Indus river–Tso Morari transect, NW Himalaya. *Journal of the Geological Society of London*, *160*(3), 385–399. https://doi.org/10.1144/0016-764902-084

Schmid, S. M., & Casey, M. (1986). Complete fabric analysis of some commonly observed quartz c-axis patterns. In B. E. Hobbs, & H. C. Heard (Eds.), *Mineral and rock deformation: Laboratory studies*, *Geophysics Monographs Series* (Vol. 36, pp. 263–286). Washington, DC: American Geophysical Union. https://doi.org/10.1029/GM036p0263

Seeber, L., & Pêcher, A. (1998). Strain partitioning along the Himalayan arc and the Nanga Parbat antiform. *Geology*, *26*(9), 791–794. https://doi.org/10.1130/0091-7613(1998)026<0791:SPATHA>2.3.CO;2

Simpson, C., & De Paor, D. G. (1993). Strain and kinematic analysis in general shear zones. *Journal of Structural Geology*, *15*(1), 1–20. https://doi.org/10.1016/0191-8141(93)90075-L

Simpson, C., & De Paor, D. G. (1997). Practical analysis of general shear zones using the porphyroclast hyperbolic distribution method: An example from the Scandinavian Caledonides. In S. Sengupta (Ed.), *Evolution of geological structures in micro- to macro-scales* (pp. 169–184). London: Chapman and Hall. https://doi.org/10.1007/978-94-011-5870-1_10

Singh, S., Kumar, R., Barley, M. E., & Jain, A. K. (2007). SHRIMP U–Pb ages and depth of emplacement of Ladakh batholith, eastern Ladakh, India. *Journal of Asian Earth Sciences*, *30*(3–4), 490–503. https://doi.org/10.1016/j.jseaes.2006.12.003

Soucy La Roche, R., Godin, L., Cottle, J. M., & Kellett, D. A. (2018). Preservation of the early evolution of the Himalayan middle crust in foreland klippen: Insights from the Karnali klippe, West Nepal. *Tectonics*, *37*, 1161–1193. https://doi.org/10.1002/2017TC004847

Spear, F. S., Kohn, M. J., & Cheney, J. T. (1999). P-T paths from anatectic pelites. *Contributions to Mineralogy and Petrology*, *134*(1), 17–32. https://doi.org/10.1007/s004100050466

Spencer, D. A., & Gebauer, D. (1996). SHRIMP evidence for a Permian age and a 44 Ma metamorphic age for the Himalayan eclogites (upper Kaghan, Pakistan): Implications for the subduction of Tethys and the subdivision terminology of the NW Himalaya. In A. M. MacFarlane, R. B. Sorkhai, J. Quade (Eds.), *11th Himalaya-Karakoram-Tibet workshop, Flagstaff, Arizona, USA, Abstracts* (pp. 147–150). Washington, DC: U.S. Government Printing Office.

St.-Onge, M. R., Rayner, N., Palin, R. M., Searle, M. P., & Waters, D. J. (2013). Integrated pressure–temperature–time constraints for the Tso Morari dome (Northwest India): Implications for the burial and exhumation path of UHP units in the western Himalaya. *Journal of Metamorphic Geology*, *31*(5), 469–504. https://doi.org/10.1111/jmg.12030

Starnes, J. K., Long, S. P., Gordon, S. M., Zhang, J., & Soignard, E. (2020). Using quartz fabric intensity parameters to delineate strain patterns across the Himalayan Main central thrust. *Journal of Structural Geology*, *131*, 103941. https://doi.org/10.1016/j.jsg.2019.103941

Steck, A., Epard, J.-L., Vannay, J.-C., Hunziker, J., Girard, M., Morard, A., & Robyr, M. (1998). Geological transect across the Tso Morari and Spiti areas: The nappe structures of the Tethys Himalaya. *Eclogae Geologicae Helveticae*, *91*, 103–121.

Steck, A., Spring, L., Vannay, J. C., Masson, H., Bucher, H., Stutz, E., et al. (1993). Geological transect across the north-western Himalaya, eastern Ladakh and Lahul (a model for the continental collision of India and Asia). *Eclogae Geologicae Helveticae*, *86*, 219–263.

Stipp, M., Stunitz, H., Heilbronner, R., & Schmid, S. M. (2002). The eastern Tonale fault zone: A 'natural laboratory' for crystal plastic deformation over a temperature range from 250° to 700°C. *Journal of Structural Geology*, *24*(12), 1861–1884. https://doi.org/10.1016/S0191-8141(02)00035-4

Stübner, K., Grujic, D., Parrish, R. R., Roberts, N. M., Kronz, A., Wooden, J., & Ahmad, T. (2014). Monazite geochronology unravels the timing of crustal thickening in NW Himalaya. *Lithos*, *210*, 111–128.

Stutz, E. A., & Steck, A. (1986). La terminaison occidentale du Cristallin du Tso Morari (Haut–Himalaya; Ladakh méridional, Inde). *Eclogae Geologicae Helveticae*, *79*, 253–269.

Stutz, E. A., & Thöni, M. (1987). The lower Paleozoic Nyimaling granite in the Indian Himalaya (Ladakh): New Rb/Sr data versus zircon typology. *Geologische Rundschau*, *76*(2), 307–315. https://doi.org/10.1007/BF01821076

Styron, R. H., Taylor, M. H., & Murphy, M. A. (2011). Oblique convergence, arc-parallel extension, and the role of strike-slip faulting in the high Himalaya. *Geosphere*, *7*(2), 582–596. https://doi.org/10.1130/GES00606.1

Suppe, J. (1983). Geometry and kinematics of fault-bend folding. *American Journal of Science*, *283*(7), 684–721. https://doi.org/10.2475/ajs.283.7.684

Thompson, A., Schulmann, K., & Jezek, J. (1997a). Extrusion tectonics and elevation of lower crustal metamorphic rocks on convergent orogens. *Geology*, *25*(6), 491–494. https://doi.org/10.1130/0091-7613(1997)025<0491:ETAEOL>2.3.CO;2

Thompson, A. B., Schulmann, K., & Jezek, J. (1997b). Thermal evolution and exhumation in obliquely convergent (transpressive) orogens. *Tectonophysics*, *280*(1–2), 171–184. https://doi.org/10.1016/S0040-1951(97)00144-3

Tikoff, B., & Fossen, H. (1995). The limitations of three-dimensional kinematic vorticity analysis. *Journal of Structural Geology*, *12*, 1771–1784.

Tonarini, S., Villa, I. M., Oberli, F., Meier, M., Spencer, D. A., Pognante, U., & Ramsay, J. R. (1993). Eocene age of eclogite metamorphism in Pakistan Himalaya: Implications for India-Eurasia collision. *Terra Nova*, *5*(1), 13–20. https://doi.org/10.1111/j.1365-3121.1993.tb00221.x

Treagus, S. H., & Treagus, J. E. (2002). Studies of strain and rheology of conglomerates. *Journal of Structural Geology*, *24*(10), 1541–1567. https://doi.org/10.1016/S0191-8141(01)00162-6

Tullis, J., & Wenk, H.-R. (1994). Effect of muscovite on the strength and lattice preferred orientations of experimentally deformed quartz aggregates. *Materials Science and Engineering*, *A175*, 209–220.

Urai, J., & Lister, W. (1986). Dynamic recrystallization of minerals. In H. Heard, & B. Hobbs (Eds.), *Mineral and Rock Deformation: Laboratory Studies*, *Geophysical Monographs* (Vol. 36, pp. 161–199). Washington, DC: American Geophysical Union.

van Daalen, M., Heilbronner, R., & Kunze, K. (1999). Orientation analysis of localized shear deformation in quartz fibres at the brittle-ductile transition. *Tectonophysics*, *303*(1–4), 83–107. https://doi.org/10.1016/S0040-1951(98)00264-9

van Hinsbergen, D. J. J., Lippert, P. C., Dupont-Nivet, G., McQuarrie, N., Doubrovine, P. V., Spakman, W., & Torsvik, T. H. (2012). Greater India Basin hypothesis and a two-stage Cenozoic collision between India and Asia. *Proceedings of the National Academy of Sciences of the United States of America*, *109*, 7659–7664. https://doi.org/10.1073/pnas.1117262109

van Hinsbergen, D. J. J., Lippert, P. C., Li, S., Huang, W., Advokaat, E. L., & Spakman, W. (2019). Reconstructing greater India: Paleogeographic, kinematic, and geodynamic perspectives. *Tectonophysics*, *760*, 69–94. https://doi.org/10.1016/j.tecto.2018.04.006

Virdi, N. S., Thakur, V. C., & Azmi, R. J. (1978). Discovery and significance of Permian microfossils in the Tso Morari Crystallines of Ladakh, Jammu and Kashmir, India. *Himalayan Geology*, *8*, 993–1000.

Vollmer, F. W. (1990). An application of eigenvalue methods to structural domain analysis. *Geological Society of America Bulletin*, *102*(6), 786–791. https://doi.org/10.1130/0016-7606(1990)102<0786:AAOEMT>2.3.CO;2

Wallis, S. R. (1992). Vorticity analysis in a metachert from the Sanbagawa Belt, SW Japan. *Journal of Structural Geology*, *14*(3), 271–280. https://doi.org/10.1016/0191-8141(92)90085-B

Wallis, S. R. (1995). Vorticity analysis and recognition of ductile extension in the Sanbagawa belt, SW Japan. *Journal of Structural Geology*, *17*(8), 1077–1093. https://doi.org/10.1016/0191-8141(95)00005-X

Walters, J. B., & Kohn, M. J. (2017). Protracted thrusting followed by late rapid cooling of the greater Himalayan sequence, Annapurna Himalaya, Central Nepal: Insights from titanite petrochronology. *Journal of Metamorphic Geology*, *35*(8), 897–917. https://doi.org/10.1111/jmg.12260

Warren, C. J., Beaumont, C., & Jamieson, R. A. (2008a). Formation and exhumation of ultra-high-pressure rocks during continental collision: Role of detachment in the subduction channel. *Geochemistry, Geophysics, Geosystems*, *9*, Q04019. https://doi.org/10.1029/2007GC001839

Warren, C. J., Beaumont, C., & Jamieson, R. A. (2008b). Modelling tectonic styles and ultra-high pressure (UHP) rock exhumation during the transition from oceanic subduction to continental collision. *Earth and Planetary Science Letters*, *267*(1–2), 129–145. https://doi.org/10.1016/j.epsl.2007.11.025

Weinberg, R. F., & Dunlap, W. J. (2000). Growth and deformation of the Ladakh batholith, Northwest Himalayas: Implications for timing of continental collision and origin of calc-alkaline batholiths. *The Journal of Geology*, *108*(3), 303–320. https://doi.org/10.1086/314405

Whipp, D. M., Beaumont, C., & Braun, J. (2014). Feeding the "aneurysm": Orogen-parallel mass transport into Nanga Parbat and the western Himalayan syntaxis. *Journal of Geophysical Research: Solid Earth*, *119*, 5077–5096. https://doi.org/10.1002/2013JB010929

White, S. (1977). Geological significance of recovery and recrystallization processes in quartz. *Tectonophysics*, *39*(1–3), 143–170. https://doi.org/10.1016/0040-1951(77)90093-2

Whitney, D. L., & Evans, B. W. (2010). Abbreviations for names of rock-forming minerals. *American Mineralogist*, *95*, 185–187.

Wilke, F. D. H., O'Brien, P. J., Gerdes, A., Timmerman, M. J., Sudo, M., & Ahmed Khan, M. (2010). The multistage exhumation history of the Kaghan Valley UHP series, NW Himalaya, Pakistan from U-Pb and $^{40}Ar/^{39}Ar$ ages. *European Journal of Mineralogy*, *22*(5), 703–719. https://doi.org/10.1127/0935-1221/2010/0022-2051

Wilke, F. D. H., O'Brien, P. J., Schmidt, A., & Ziemann, M. A. (2015). Subduction, peak and multi-stage exhumation metamorphism: Traces from one coesite-bearing eclogite, Tso Morari, western Himalaya. *Lithos*, *231*, 77–91. https://doi.org/10.1016/j.lithos.2015.06.007

Xypolias, P. (2009). Some new aspects of kinematic vorticity analysis in naturally deformed quartzites. *Journal of Structural Geology*, *31*(1), 3–10. https://doi.org/10.1016/j.jsg.2008.09.009

Xypolias, P. (2010). Vorticity analysis in shear zones: A review of methods and applications. *Journal of Structural Geology*, *32*(12), 2072–2092. https://doi.org/10.1016/j.jsg.2010.08.009

Xypolias, P., Spanos, D., Chatzaras, V., Kokkalas, S., & Koukouvelas, I. (2010). Vorticity of flow in ductile thrust zones: Examples from the Attico-Cycladic massif (internal Hellenides, Greece). In R. D. Law, R. W. H. Butler, R. Holdsworth, M. Krabbendam, R. A. Strachan (Eds.), *Continental Tectonics and Mountain Building - the Legacy of Peach and Horne*, *Special Publication* (Vol. 335, pp. 687–714). London: Geological Society. https://doi.org/10.1144/SP335.24

Yin, A. (2006). Cenozoic tectonic evolution of the Himalayan orogen as constrained by along-strike variation of structural geometry, exhumation history, and foreland sedimentation. *Earth Science Reviews*, *76*(1–2), 1–131. https://doi.org/10.1016/j.earscirev.2005.05.004

Yonkee, W. A., Czeck, D. M., Nachbor, A. C., Barszewski, C., Pantone, S., Balgord, E. A., & Johnson, K. R. (2013). Strain accumulation and fluid-rock interaction in a naturally deformed diamictite, Willard thrust system, Utah (USA): Implications for crustal rheology and strain softening. *Journal of Structural Geology*, *50*, 91–118. https://doi.org/10.1016/j.jsg.2012.10.012

Zhang, Z., Xiang, H., Dong, X., Ding, H., & He, Z. (2015). Long-lived high-temperature granulite-facies metamorphism in the eastern Himalayan orogen, south Tibet. *Lithos*, *212–215*, 1–15. https://doi.org/10.1016/j.lithos.2014.10.009